Journal of *Marine Science and Engineering*

MDPI

Article

Modeling, Control and Experiments of a Novel Underwater Vehicle with Dual Operating Modes for Oceanographic Observation

Junjun Cao, Rui Lin, Baoheng Yao, Chunhu Liu, Xiaochao Zhang and Lian Lian *

School of Oceanography, Shanghai Jiao Tong University, B105 Mu Lan Building, 800 Dongchuan Road, Shanghai 200240, China; cpcjj19890318@sjtu.edu.cn (J.C.); linrui0213@sjtu.edu.cn (R.L.); yaobaoheng@sjtu.edu.cn (B.Y.); liuchunhu@sjtu.edu.cn (C.L.); zhangxiaochao2005@126.com (X.Z.)
* Correspondence: llian@sjtu.edu.cn; Tel.: +86-1881-789-3512

Abstract: Multifarious and continuous oceanographic observation data is of considerable significance to oceanographic research and military application. In this paper, a novel oceanographic observation method with dual-modal underwater vehicle able to switch between the Argo and Glider modes is proposed and is studied experimentally in the South China Sea. Using the Newton–Euler formulation, a complete dynamic model considering the variation in gravity/buoyancy due to mode switching is thus established. Then, based on Lyapunov stability criterion, a nonlinear adaptive inverse controller with multiple inputs and multiple outputs is developed which enables the observation platform to freely switch between various modes. By analyzing the numerical and experimental data of a single mode, the results demonstrate that the proposed method can supplement the observation data and improve the accuracy of oceanographic data. Finally, based on experimental data acquired by the dual-modal underwater vehicle in the South China Sea, three-dimensional regional oceanic temperature and salinity fields are constructed with the spatio-temporal Kriging method, and feature surfaces are extracted from the oceanic fields. Furthermore, the proposed method can be applied in other stirring dynamic regions, such as ocean eddies, ocean fronts, filaments, etc.

Keywords: dual-modal underwater vehicle; dynamic modeling; adaptive motion control; oceanic element field construction; South China Sea

check for updates

Citation: Cao, J.; Lin, R.; Yao, B.; Liu, C.; Zhang, X.; Lian, L. Modeling, Control and Experiments of a Novel Underwater Vehicle with Dual Operating Modes for Oceanographic Observation. *J. Mar. Sci. Eng.* **2022**, *10*, 921. https://doi.org/10.3390/jmse10070921

Academic Editors: Mohamed Benbouzid and Alessandro Ridolfi

Received: 30 May 2022
Accepted: 1 July 2022
Published: 3 July 2022

Publisher's Note: MDPI stays neutral with regard to jurisdictional claims in published maps and institutional affiliations.

Copyright: © 2022 by the authors. Licensee MDPI, Basel, Switzerland. This article is an open access article distributed under the terms and conditions of the Creative Commons Attribution (CC BY) license (https://creativecommons.org/licenses/by/4.0/).

1. Introduction

Oceanographic observation is the foundation of marine science research and is one of the most critical factors in maritime strategy. Due to the low consumption and long-range transport capacities with high spatial-temporal resolution, unmanned underwater vehicles have a significant competitive advantage over measures with prior technology [1]; the profiling Argos [2] and underwater gliders [3] are widely used in oceanographic observation.

As for the current Argos, they have been experimentally verified as having the ability of sustaining effort for three or even five years, which is assessed by its low-consumption driven system. Nevertheless, the Argo can only drift with the currents without maneuvering, which makes the position of the Argo uncontrollable and difficult to predict. Underwater gliders, a kind of autonomous underwater vehicle with maneuverability, have shown powerful performance in sampling and exploring the ocean environment. Despite the underwater gliders being robust sampling platforms which are increasingly deployed in some complex current regions, their endurance is often limited to about 3 to 6 months depending on the battery capacity and the operating mode. In addition, the endurance of underwater gliders is significantly inferior to profiling drifting float.

Although existing vehicles have many important applications, the vehicles with a single operating mode cannot satisfy the needs of comprehensive observation. A desired ocean-observing platform would have the combined positive attributes of an underwater

glider and the long endurance as an Argo profiling float. Multifarious and continuous observation data can be achieved by a novel dual-modal underwater vehicle, which integrates the concept of buoyancy-driven underwater gliders and conventional profiling floats [4]. Such a dual-modal vehicle would merge the benefits of taking measurements in a very energy-efficient way when drifting with the currents in Argo mode, and operating as an underwater glider in glider mode when it is needed to cross the ocean eddies, ocean fronts, filaments, or some other stirring dynamic regions [5–7].

DUV (dual-modal underwater vehicle) is a mobile observation platform that combines Argo and Glider working modes. It possesses both the vertical profile capability of Argo long-term observation and the sawtooth glide observation capability of Glider large/medium-scale navigation with high work efficiency, and long endurance and observation range. Therefore, the mission of ocean monitoring and exploration can be completed effectively and to a high standard. The typical operating scenarios and processes of DUV are shown in Figure 1. DUV can perform long-term and low-power vertical profile motions in the target sea area in Argo mode, and monitor the surrounding marine environment with sensors. When the target area, phenomenon or object is observed or detected, the platform switches to Glider mode to perform tasks such as area monitoring or target tracking. After completing the missions, it switches to low-power Argo mode for routine monitoring. The capability to operate in each mode and the capability to switch modes will directly affect the feasibility of mission execution and the integrity of data observation.

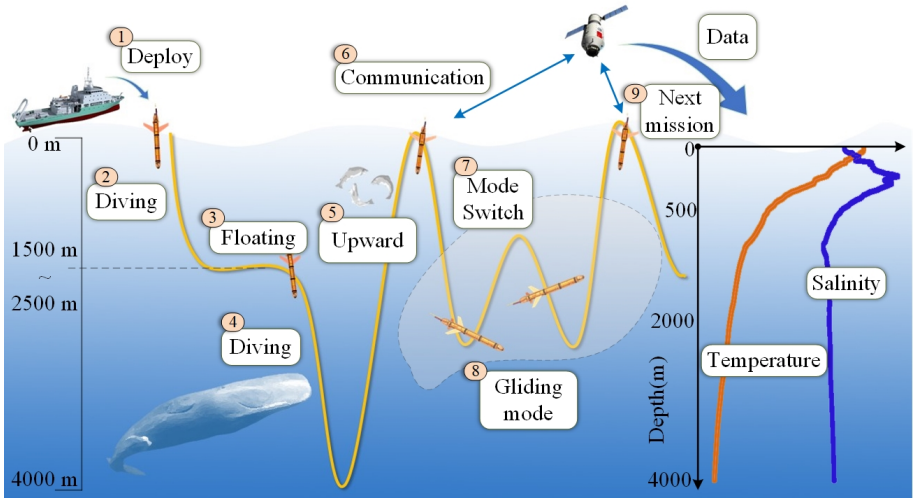


Figure 1. Typical work processes of DUV.

The dynamic model of an underwater vehicle has been widely used in the analysis of the motion characteristics of vehicles and research into navigation control technology [8,9]. The model of Glider has developed rapidly and made significant progress, which is represented in the research of nonlinear dynamics [10]. Based on the Newton–Euler equation, a simplified kinetic model was established by Graver and Leonard et al. [11]. The Glider was regarded as a combination of dual particles. The Glider's dynamic model was deduced and the impacts of particle weight and moving distance were analysed in detail. Wang, Y.H. and Wang S.X. et al. [12–14] changed the translational motion of the movable mass in the Glider by three degrees of freedom to the eccentric mass rotation and the translational motion of the heavy object that were closer to the actual application, and established a more accurate kinetic model of Glider based on the Gibbs–Appel equation. The causality relationship between the actuator and the properties of the vehicle were analyzed. Fan, S.S. [15] established a complete kinetic model of a multi-body glider system under the influence of ocean currents, and the influence of ocean-current velocity gradient on the dynamic behavior of glider was considered emphatically. However, the single-mode kinetic model of Glider cannot describe the motion characteristics of dual-modal coupling.

The research on the dynamic model of DUV is still in its infancy, and further research is needed on the coupling effect of each actuator on the system.

Controlling underwater gliders is a topic that has been widely researched, and a variety of approaches have been developed and applied to the attitude-control problem, such as sliding mode control, linear-quadratic regular control, predictive control, adaptive control and so on. However, the novel vehicle creates new problems for the system control of sub-driven systems. The control input and control law of the DUV system will change with the transformations in the motion attitude and motion mode during the navigation process. Therefore, switching motion control is the key to the safety and stable operation of DUV.

According to the literature survey, multi-mode switching control is mainly used in the field of flight control, and only a few researchers are engaged in the research around the switching motion control of DUV. The concept of transition speed domain for the three-dimensional path-tracking problem of an AUV (autonomous underwater vehicle) was proposed by Breivik et al. [16], who designed weighted variables to make the lateral speed transition smoothly. A tanh-type switching function was designed by Xiang, X., Yu C. et al. [17] for position and attitude switching in the transition speed domain, and they realized the position and attitude soft switching variable speed path-tracking control of an AUV in the full speed domain. Niu W.D. [18] studied the relationship between the control input and the motion characteristics of an HUG (hybrid underwater vehicle) under different driving modes, and designed linear and nonlinear controllers in the longitudinal plane based on the nonlinear dynamic inverse method, and implemented the multi-model method in switching controls to realize switching in the two modes of glide and hybrid drive. In addition, based on a hybrid drive glider, the performances of the LQR and PID controllers were compared and analyzed in detail by Noh [19] and Isa [20], and the neural-network predictive controller and model predictive controller was also designed to smooth the control input. Based on the parametric uncertainty model, a robust $H\infty$ controller was designed by Wang S.X. [21] and Wang Y.H. [22] to ensure the operating performance of the vehicle under the disturbance. In sliding mode control, an output-tracking robust controller was designed by Ma J. and Liu Y.J. [23,24] to make the system robust to parameter changes and disturbances. Cao J.L. and Cao J.J. [25] designed an adaptive controller based on Lyapunov stability criterion to make the glider able to adjust its attitude during movement.

During the switching-control process, the system would produce a large attitude angle, and switch from one-dimensional motion to three-dimensional motion [26]. The above research work is not comprehensive enough to analyze the motion stability of the underwater platform during the mode-switching process. Considering the sudden change in degrees of freedom such as heading, and the influence of external and internal factors, the switching-control motion and navigation process of DUV deserved further study. The main contributions of this work are as follows: Firstly, based on the principle design of DUV, in this paper a whole system kinetics model of DUV is established by considering the commonalities and differences of the working modes of Argo and Glider. Secondly, a multi-input and multi-output nonlinear adaptive control algorithm is proposed to solve the dynamic variations in the control input that are caused by the mode switching of the DUV. The stability of the system was verified by the Lyapunov stability criterion, and simulation analysis was carried out. In addition, we also conducted sea trials to check various performances of DUV, further carried out networking experiments, and used the spatio-temporal Kriging method to reconstruct the three-dimensional temperature and salinity fields of the ocean, which verified the feasibility and effectiveness of DUV.

The remainder of the paper is organized as follows. The dynamic model steered by internal movable and rotary mass is derived in Section 2. Then the MIMO ABC (multi-input and multi-output adaptive backstepping control) controller designing process and Lyapunov stability verification are introduced in Section 3. The next section presents the characteristics and analysis of dual-modal motion for the vehicle. Section 5 presents the experiment results. Finally, Section 6 draws the conclusion of the work.

2. Dynamic Model for the Dual-Modal Underwater Vehicle

The multimodal underwater vehicle is designed to obtain multifarious and continuous oceanographic data. It can achieve a large change in the center of the mass of the vehicle by adjusting the 360° rotation of the mass block, thereby realizing the switching of the Argo and Glider motion modes. During the descent process, the horizontal movement is achieved by two wings close to the tail. The detailed configuration of the DUV is shown in Figure 2. The main components and subsystems design, and the correlative mathematical analysis are introduced in detail in [26]. The parameters of the vehicle are listed in Table A1. The interior of the DUV tail fairing is equipped with an emergency ejection system and a hydrophone, and the satellite communication antenna is fitted on the mast platform at the end of DUV. In this section, the kinetics mode of DUV driven by an internal buoyancy system and steered by a movable and rotatable battery pack is established. The explanations of the symbols used in this paper are described in Table A2.

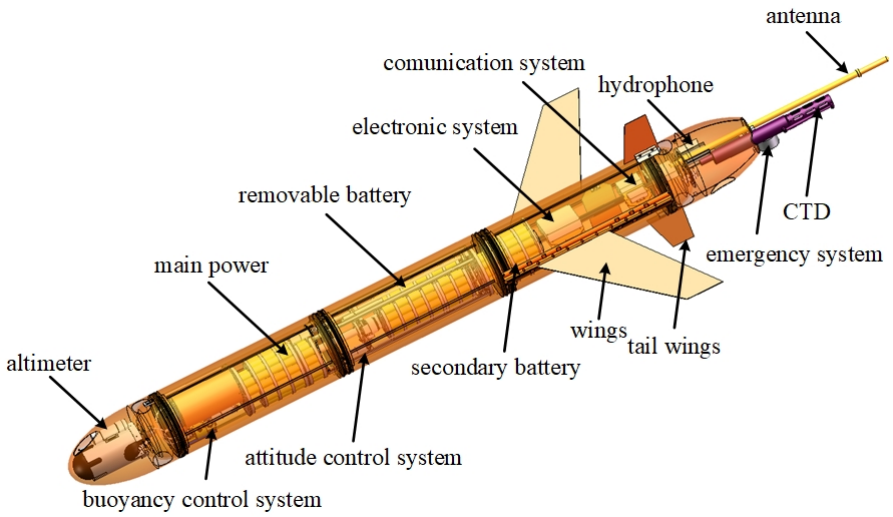


Figure 2. Configurations of the DUV.

2.1. Coordinate Frames

In this paper, to simplify the dynamic system and analytical process, the multi-body coordinate system of DUV is established by referring to the traditional establishing method which ignored the curvature of the Earth's surface, including inertial frame(navigation frame), body frame and flow frame, as shown in Figure 3. The definition of the frame used and the definition of related variables in this paper are defined by the symbol system recommended by the International Towing Pool Association (ITTC). The inertial frame is represented by $\mathbf{E_0} - \mathbf{ijk}$, where $\mathbf{E_0}$ is the origin of the frame; $\mathbf{i}, \mathbf{j}, \mathbf{k}$ are the unit vectors in three directions and the three vectors conform to the right-hand rule; $\mathbf{i}, \mathbf{j}$ are perpendicular to each other to form a horizontal plane (sea level, $z = 0$). The direction of $\mathbf{k}$ is vertically downward along the direction of the gravitational acceleration g. The navigation position of the underwater vehicle is represented by the coordinate of its geometric centroid in the inertial system named $\mathbf{b}$, where $\mathbf{b} = [x, y, z]^T$, $(x, y, z, \phi, \theta, \psi)$ represents the position and Euler angles of the vehicle in the inertial frame. The origin $\mathbf{B_0}$ of the body frame coincides with the position of the buoyancy center of the underwater vehicle. The position of the body frame in the inertial system is the position of the underwater vehicle $\mathbf{b}$. The three-unit vectors of the body frame are represented as $\mathbf{e_0}, \mathbf{e_1}, \mathbf{e_2}$. Here, $\mathbf{e_0}$ points to the bow of the vehicle along the direction of the central axis, $\mathbf{e_1}$ is perpendicular to $\mathbf{e_0}$, pointing to the right side of the vehicle, and $\mathbf{e_2}$ is perpendicular to the plane composed of $\mathbf{e_1}$ and $\mathbf{e_0}$, pointing to the bottom of the vehicle. The velocity and angular velocity of the vehicle in the body frame are $\mathbf{V} = [u, v, w]^T$ and $\mathbf{\Omega} = [p, q, r]^T$. The force $\mathbf{F} = [X, Y, Z]^T$ and moment $\mathbf{T} = [K, M, N]^T$ are all variables presented in body coordinates.

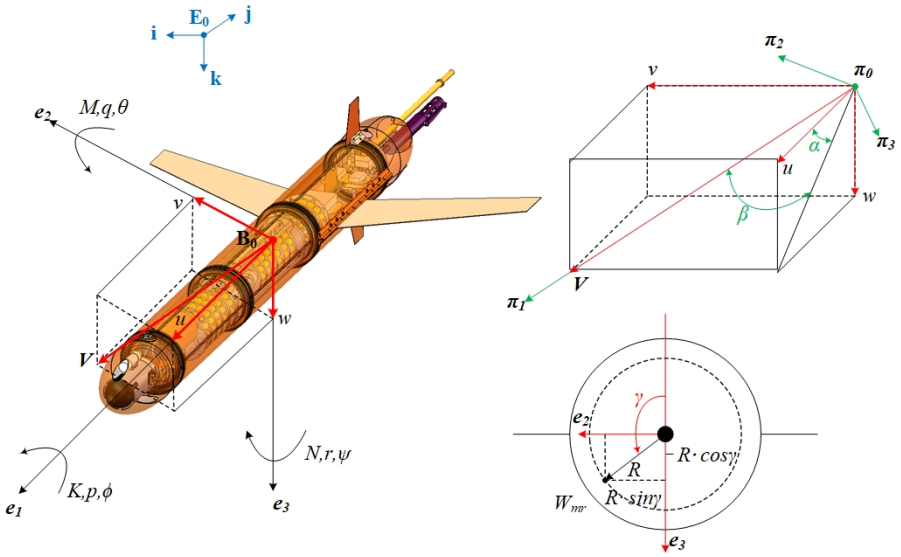


Figure 3. The frames of the dynamic model.

Generally, the variables in the inertial frame and the variables in the body frame can be mapped to each other through a mapping relationship, as shown in Equation (1).

$$\dot{\mathbf{b}} = \mathbf{R}_{EB}\mathbf{V} \tag{1}$$

where $\mathbf{R}_{EB}$ is the coordinate rotation matrix, which means the variables in the body coordinates are mapped to the inertial frame, and the rotation order follows the aviation order. Its expression is shown as follows.

$$\mathbf{R}_{EB} = \begin{bmatrix} \cos\theta\cos\psi & \sin\phi\sin\theta\cos\psi - \cos\phi\sin\psi & \cos\phi\sin\theta\cos\psi + \sin\phi\sin\psi \\ \cos\theta\sin\psi & \cos\phi\cos\psi + \sin\phi\sin\theta\sin\psi & -\sin\phi\cos\psi + \cos\phi\sin\theta\sin\psi \\ -\sin\theta & \sin\phi\cos\theta & \cos\phi\cos\theta \end{bmatrix}$$

Similarly, there is a similar mapping relationship between the Euler angle $\boldsymbol{\theta}$ in the inertial system and the angular velocity $\boldsymbol{\Omega}$ in the body frame, as shown in Equation (2). The degradation phenomenon occurs when the Euler angle θ is close to $\pm 90^{\circ}$. The gimbal deadlock problem occurs when θ is equal to 90°, but DUV includes a vertical attitude of $\theta = 90^{\circ}$ during the switching of the operating mode. In order to accurately describe the change in attitude of the observation platform, the quaternion method needs to be used instead of the Euler-angle description method.

$$\dot{\boldsymbol{\theta}} = \begin{bmatrix} 1 & \sin\phi\tan\theta & \cos\phi\tan\theta \\ 0 & \cos\phi & -\sin\phi \\ 0 & \sin\phi\sec\theta & \cos\phi\sec\theta \end{bmatrix} \boldsymbol{\Omega} \tag{2}$$

The magnitude and direction of the force and moment of the vehicle moving in water are mainly related to the speed of the vehicle. $\mathbf{V_r}$ is used to represent the speed of the vehicle relative to the water flow. The flow velocity frame is defined as $\boldsymbol{\pi_0 - \pi_1\pi_2\pi_3}$. The origin $\boldsymbol{\pi_0}$ coincides with the origin of the body frame. Three units vectors $\boldsymbol{\pi_1, \pi_2, \pi_3}$ represent the three directions of the frame. $\boldsymbol{\pi_1}$ points to the direction of the vehicle velocity $\mathbf{V_r}$. The body coordinates can be mapped to the flow velocity coordinates through the following two rotation steps, and the rotation matrix is $\mathbf{R}_{\pi B}$.

1. Rotate the body frame around the $\mathbf{e_2}$ axis by $-\alpha$, then the $\mathbf{e_3}$ axis coincides with the $\boldsymbol{\pi_3}$ axis;
2. Rotate the frame around the $\boldsymbol{\pi_3}$ axis by β, then the $\mathbf{e_1}$ axis coincides with the $\boldsymbol{\pi_1}$ axis, and the $\mathbf{e_2}$ axis coincides with the $\boldsymbol{\pi_2}$ axis.

$$\mathbf{R}_{\pi B} = \begin{bmatrix} \cos\alpha\cos\beta & \sin\beta & \sin\alpha\cos\beta \\ -\cos\alpha\sin\beta & \cos\beta & -\sin\alpha\sin\beta \\ -\sin\alpha & 0 & \cos\alpha \end{bmatrix}$$

α and β are, respectively, the attack angle and drift angle of the vehicle during the gliding process, which are specifically defined as Equation (3).

$$\begin{aligned} \alpha &= \tan^{-1}\frac{v_{r3}}{v_{r1}} \\ \beta &= \sin^{-1}\frac{v_{r2}}{\|\mathbf{V_r}\|} \end{aligned} \tag{3}$$

where $\mathbf{V_r} = [v_{r1}, v_{r2}, v_{r3}]^T$; v_{r1}, v_{r2}, v_{r3} represent the velocity components of the vehicle in flow velocity frame with respect to current; and $\mathbf{V_r} = \mathbf{V}$ in a still-water environment.

2.2. Model of Mechanics

The mass of DUV is divided into three parts: fixed mass m_{rb}, moving mass m_{mr} and variable mass m_b. Fixed mass m_{rb} includes parts with fixed positions such as pressure shells, wings, fixed batteries, fasteners and control systems, which are regarded as rigid mass points during the modeling, and their positions in the body frame are represented as $\mathbf{r}_{rb}$; in the inertial frame they are represented as $\mathbf{r}_{rbE}$. The moving mass m_{mr} is the mass of the eccentric mass block in the attitude-adjustment system, which can perform translational and rotational movements. It can be regarded as a mass point with constant mass and variable position, which position in the vehicle frame is represented as $\mathbf{r}_{mr}$, and position in the inertial frame is represented as $\mathbf{r}_{mrE}$. The variable mass m_b is the adjustable mass of the buoyancy adjustment system, which can control the vehicle's diving and floating upward by adjusting the buoyancy of the vehicle. It is regarded as a mass point with constant position and variable mass, whose position in the vehicle frame is represented as $\mathbf{r}_b$, and whose position in the inertial frame is represented as $\mathbf{r}_{bE}$. The total displacement mass of the DUV is expressed as m, $m = m_{rb} + m_{mr} + m_b$. The total mass of the DUV remains constant during the modeling , which is represented as m_d. The net mass (net buoyancy) of the vehicle in the water during the modeling is represented as m_0.

$$m_0 = m - m_d = m_{rb} + m_{mr} + m_b - m_d \tag{4}$$

Reference [11] defines the operator $\hat{\cdot}$. For any vector $\boldsymbol{x} = [x_1, x_2, x_3]^T$, Equation (5) can be obtained after expansion. For any two vectors $\boldsymbol{x} = [x_1, x_2, x_3]^T$ and $\boldsymbol{y} = [y_1, y_2, y_3]^T$, $\hat{\boldsymbol{x}}\boldsymbol{y} = \boldsymbol{x} \times \boldsymbol{y}$.

$$\hat{\boldsymbol{x}} = \begin{bmatrix} 0 & -x_3 & x_2 \\ x_3 & 0 & -x_1 \\ -x_2 & x_1 & 0 \end{bmatrix} \tag{5}$$

Through the velocity and angular velocity calculation formulas of theoretical mechanics, the velocity and angular velocity of fixed mass and variable mass in the inertial frame can be expressed as Equations (6) and (7).

$$\begin{aligned} \mathbf{V}_{rb} &= \mathbf{V} + \dot{\mathbf{r}}_{rb} - \hat{\mathbf{r}}_{rb}\boldsymbol{\Omega}_{rb} \\ \boldsymbol{\Omega}_{rb} &= \boldsymbol{\Omega} \end{aligned} \tag{6}$$

$$\begin{aligned} \mathbf{V}_b &= \mathbf{V} + \dot{\mathbf{r}}_b - \hat{\mathbf{r}}_b\boldsymbol{\Omega}_b \\ \boldsymbol{\Omega}_b &= \boldsymbol{\Omega} \end{aligned} \tag{7}$$

The motion of the attitude-adjustment system studied in this paper consists of two parts, which are divided into the axial motion of the slider in the direction of $\mathbf{e_1}$ and the rotational motion around the axis $\mathbf{e_1}$. As shown in Figure 3, the displacement of the moveable mass along the $\mathbf{e_1}$ axis in the vehicle frame is represented as r_{mrx}. The rotation angle of the moveable mass around the $\mathbf{e_1}$ axis in the vehicle frame is represented as γ. The eccentric

distance of the moveable mass is represented as R_{mr}. According to the relevant introduction of the literature [26], the attitude-adjustment system is the critical factor during the DUV modeling. The DUV is operating in Glider mode when γ changes between $[-90°, 90°]$. When $\gamma = 180°$, the moment generated by the eccentric mass m_{mr} and the righting moment generated by the remaining fixed mass m_{rb} cancel each other out, then the center of gravity and the center of buoyancy of the DUV are both on the x axis. The vehicle is now in vertical state. The eccentric moments generated by the eccentric mass and the remaining fixed mass are equal. Therefore, the position $\mathbf{r}_{mr}$ of the moveable mass in the vehicle frame can be expressed by Equation (8). The velocity and angular velocity of the attitude adjustment system in the inertial system are expressed by Equation (9).

$$\mathbf{r}_{mr} = \left[r_{mrx}, R_{mr}\cos(\gamma + \frac{\pi}{2}), R_{mr}\sin(\gamma + \frac{\pi}{2}) \right]^T \tag{8}$$

$$\begin{aligned} \mathbf{V}_{mr} &= \mathbf{V} + \dot{\mathbf{r}}_m r - \hat{\mathbf{r}}_{mr}\boldsymbol{\Omega}_{mr} \\ \boldsymbol{\Omega}_{mr} &= \boldsymbol{\Omega} + \dot{\gamma}\mathbf{e_1} \end{aligned} \tag{9}$$

The inertia matrix of the particle is an indispensable parameter for analyzing the motion of the particle system. In this paper, the rotational inertia matrix of fixed mass, variable mass and moveable/rotateable mass are represented as $\mathbf{I}_{rb}$, $\mathbf{I}_b$ and $\mathbf{I}_{mr}$, as shown in Equation (10), respectively.

$$\begin{aligned} \mathbf{I}_{rb} &= -m_{rb}\hat{\mathbf{r}}_{rb}\hat{\mathbf{r}}_{rb} \\ \mathbf{I}_b &= -m_b\hat{\mathbf{r}}_b\hat{\mathbf{r}}_b \\ \mathbf{I}_{mr} &= \mathbf{R}_{e1}^T(\gamma)\mathbf{I}_{mr}^0\mathbf{R}_{e1}(\gamma) \end{aligned} \tag{10}$$

where $\mathbf{R}_{e1}$ is the mapping matrix that rotates around the $\mathbf{e_1}$ axis, $\mathbf{I}_{mr}^0$ is the initial inertia matrix when $\gamma = 0$, as shown below. $\mathbf{I}_{rb}$ is a constant, and $\mathbf{I}_b$ varies with m_b, $\mathbf{I}_{mr}$ varies with r_{mrx} and γ.

$$\mathbf{R}_{e1}(\gamma) = \begin{bmatrix} 1 & 0 & 0 \\ 0 & \cos\gamma & -\sin\gamma \\ 0 & \sin\gamma & \cos\gamma \end{bmatrix}$$

$$\mathbf{I}_{mr}^0 = \mathrm{m}_{mr}\begin{bmatrix} {R_{mr}}^2 & 0 & -r_{mrx}R_{mr} \\ 0 & {r_{mrx}}^2 + {R_{mr}}^2 & 0 \\ -r_{mrx}R_{mr} & 0 & {r_{mrx}}^2 \end{bmatrix}$$

2.3. Dynamic Model

The force and moment acting on the vehicle by the external environment are represented as $\mathbf{f}_{ext}$ and $\boldsymbol{\tau}_{ext}$. The force $\mathbf{F}$ and moment $\mathbf{T}$ of the vehicle in the vehicle frame can be obtained by coordinate transformation, as shown in Equation (11).

$$\begin{aligned} \mathbf{F} &= \mathbf{R}_{\mathrm{EB}}^{\mathrm{T}}\mathbf{f}_{ext} \\ \mathbf{T} &= \mathbf{R}_{\mathrm{EB}}^{\mathrm{T}}\boldsymbol{\tau}_{ext} \end{aligned} \tag{11}$$

The momentum and angular momentum of the vehicle in the inertial frame are represented as $\mathbf{p}$ and $\boldsymbol{\pi}$. The momentum and angular momentum of the vehicle in the vehicle frame are represented as $\mathbf{P}$ and $\boldsymbol{\Pi}$. The momentum/angular momentum in the vehicle frame and the momentum/angular momentum in the inertial frame have the conversion relationship of Equation (12). Equation (13) can obtained by taking the derivative with respect to time of Equation (12).

$$\begin{aligned} \mathbf{p} &= \mathbf{R}_{\mathrm{EB}}\mathbf{P} \\ \boldsymbol{\pi} &= \mathbf{R}_{\mathrm{EB}}\boldsymbol{\Pi} + \hat{\mathbf{b}}\mathbf{p} \end{aligned} \tag{12}$$

$$\begin{aligned} \dot{\mathbf{p}} &= \mathbf{R}_{\mathrm{EB}}(\dot{\mathbf{P}} + \hat{\boldsymbol{\Omega}}\mathbf{P}) \\ \dot{\boldsymbol{\pi}} &= \mathbf{R}_{\mathrm{EB}}(\dot{\mathbf{\Pi}} + \hat{\boldsymbol{\Omega}}\boldsymbol{\Pi}) + \mathbf{R}_{\mathrm{EB}}\hat{\mathbf{V}}\mathbf{p} + \dot{\mathbf{b}}\hat{\mathbf{p}} \end{aligned} \tag{13}$$

According to the momentum theorem, the forces and moments of the vehicle during the movement can be calculated by Equation (14).

$$\begin{aligned} \dot{\mathbf{p}} &= (m_{rb} + m_{mr} + m_b - m_d)\mathrm{g}\mathbf{k} + \mathbf{f}_{ext} \\ \dot{\boldsymbol{\pi}} &= m_{rb}\mathrm{g}\hat{\mathbf{r}}_{rbE}\mathbf{k} + m_{mr}\mathrm{g}\hat{\mathbf{r}}_{pE}\mathbf{k} + m_b\mathrm{g}\hat{\mathbf{r}}_{bE}\mathbf{k} + \boldsymbol{\tau}_{ext} \end{aligned} \tag{14}$$

where $\mathbf{r}_{rbE}$, $\mathbf{r}_{mrE}$ and $\mathbf{r}_{bE}$ are the positions of fixed mass, moving mass, and variable mass in the inertial frame. Substituting Equation (14) into Equation (13), the force and moment of the vehicle in the vehicle frame are obtained as Equation (15).

$$\begin{aligned} \dot{\mathbf{P}} &= \hat{\mathbf{P}}\boldsymbol{\Omega} + \mathbf{R}_{\mathrm{EB}}^{\mathrm{T}}(m_{rb} + m_{mr} + m_b - m_d)\mathrm{g}\mathbf{k} + \mathbf{F} \\ \dot{\mathbf{\Pi}} &= \hat{\mathbf{\Pi}}\boldsymbol{\Omega} + \hat{\mathbf{P}}\mathbf{V} + (m_{rb}\mathbf{r}_{rb} + m_{mr}\mathbf{r}_{mr} + m_b\mathbf{r}_b)\mathrm{g} \times (\mathbf{R}_{\mathrm{EB}}^{\mathrm{T}}\mathbf{k}) + \mathbf{T} \end{aligned} \tag{15}$$

The equations of $\mathbf{P}$ and $\boldsymbol{\Pi}$ with respect to $\mathbf{V}$ and $\boldsymbol{\Omega}$ are obtained according to the method of taking the derivative with respect to kinetic energy by [11]. The kinetic energy of DUV is divided into four parts: fixed mass kinetic energy, moving mass kinetic energy, variable mass kinetic energy and additional mass kinetic energy. The kinetic energy of the particle system can be calculated by Equation (16).

$$T = \sum_{i=0}^{n} T_i = \sum_{i=0}^{n} \frac{1}{2} m_i \|\mathbf{V}_i\|^2 + \frac{1}{2}\boldsymbol{\Omega}_i^T \mathbf{I}_i \boldsymbol{\Omega}_i \tag{16}$$

The fixed mass kinetic energy T_{rb}, the moving mass kinetic energy T_{mr}, the variable mass kinetic energy T_b and the additional mass kinetic energy T_f can be calculated, respectively, according to the particle kinetic energy theorem, as Equations (17) and (18).

$$\begin{aligned} T_{rb} &= \frac{1}{2}\begin{bmatrix} \mathbf{V} \\ \boldsymbol{\Omega} \\ \dot{\mathbf{r}}_{rb} \end{bmatrix}^{\mathrm{T}} \begin{bmatrix} m_{rb}\boldsymbol{\mathcal{I}} & -m_{rb}\hat{\mathbf{r}}_{rb} & m_{rb}\boldsymbol{\mathcal{I}} \\ m_{rb}\hat{\mathbf{r}}_{rb} & \mathbf{I}_{rb} - m_{rb}\hat{\mathbf{r}}_{rb}\hat{\mathbf{r}}_{rb} & m_{rb}\hat{\mathbf{r}}_{rb} \\ m_{rb}\boldsymbol{\mathcal{I}} & -m_{rb}\hat{\mathbf{r}}_{rb} & m_{rb}\boldsymbol{\mathcal{I}} \end{bmatrix} \begin{bmatrix} \mathbf{V} \\ \boldsymbol{\Omega} \\ \dot{\mathbf{r}}_{rb} \end{bmatrix} \\ T_{mr} &= \frac{1}{2}\begin{bmatrix} \mathbf{V} \\ \boldsymbol{\Omega}_{mr} \\ \dot{\mathbf{r}}_{mr} \end{bmatrix}^{\mathrm{T}} \begin{bmatrix} m_{mr}\boldsymbol{\mathcal{I}} & -m_{mr}\hat{\mathbf{r}}_{mr} & m_{mr}\boldsymbol{\mathcal{I}} \\ m_{mr}\hat{\mathbf{r}}_{mr} & \mathbf{I}_{mr} - m_p\hat{\mathbf{r}}_{mr}\hat{\mathbf{r}}_{mr} & m_{mr}\hat{\mathbf{r}}_{mr} \\ m_{mr}\boldsymbol{\mathcal{I}} & -m_{mr}\hat{\mathbf{r}}_{mr} & m_{mr}\boldsymbol{\mathcal{I}} \end{bmatrix} \begin{bmatrix} \mathbf{V} \\ \boldsymbol{\Omega}_{mr} \\ \dot{\mathbf{r}}_{mr} \end{bmatrix} \\ T_b &= \frac{1}{2}\begin{bmatrix} \mathbf{V} \\ \boldsymbol{\Omega} \\ \dot{\mathbf{r}}_b \end{bmatrix}^{\mathrm{T}} \begin{bmatrix} m_b\boldsymbol{\mathcal{I}} & -m_b\hat{\mathbf{r}}_b & m_b\boldsymbol{\mathcal{I}} \\ m_b\hat{\mathbf{r}}_b & \mathbf{I}_b - m_b\hat{\mathbf{r}}_b\hat{\mathbf{r}}_b & m_b\hat{\mathbf{r}}_b \\ m_b\boldsymbol{\mathcal{I}} & -m_b\hat{\mathbf{r}}_b & m_b\boldsymbol{\mathcal{I}} \end{bmatrix} \begin{bmatrix} \mathbf{V} \\ \boldsymbol{\Omega} \\ \dot{\mathbf{r}}_b \end{bmatrix} \end{aligned} \tag{17}$$

$$T_f = \frac{1}{2}\begin{bmatrix} \mathbf{V} \\ \boldsymbol{\Omega} \end{bmatrix}^{\mathrm{T}} \begin{bmatrix} \mathbf{M}_f & \mathbf{D}_f^{\mathrm{T}} \\ \mathbf{D}_f & \mathbf{I}_f \end{bmatrix} \begin{bmatrix} \mathbf{V} \\ \boldsymbol{\Omega} \end{bmatrix} \tag{18}$$

where $\boldsymbol{\mathcal{I}}$ represents the 3×3 identity matrix. $\mathbf{M}_f$ is the additional mass matrix of the vehicle; $\mathbf{I}_f$ is the additional inertia matrix; $\mathbf{D}_f$ is the coupling term of the vehicle due to translation and rotation, including the Coriolis force matrix and the centripetal force matrix. Due to the slow rotation of the rolling mechanism of the vehicle, the value of $\dot{\gamma}$ is small enough to be ignored. Thereby, the kinetic energy of the vehicle particle system can be calculated by Equation (19).

$$T = T_{rb} + T_{mr} + T_b + T_f = \frac{1}{2}\begin{bmatrix} \mathbf{V} \\ \mathbf{\Omega} \\ \dot{\mathbf{r}}_{rb} \\ \dot{\mathbf{r}}_{mr} \\ \dot{\mathbf{r}}_b \end{bmatrix}^{\mathrm{T}} \mathbf{\Gamma} \begin{bmatrix} \mathbf{V} \\ \mathbf{\Omega} \\ \dot{\mathbf{r}}_{rb} \\ \dot{\mathbf{r}}_{mr} \\ \dot{\mathbf{r}}_b \end{bmatrix} \tag{19}$$

The generalized mass matrix of the vehicle particle system and the additional mass can be represented as $\mathbf{\Gamma}$.

$$\mathbf{\Gamma} = \begin{bmatrix} \mathbf{M}_f + m\boldsymbol{\mathcal{I}} & \mathbf{D}_f - \tilde{m}\tilde{\mathbf{r}} & m_{rb}\boldsymbol{\mathcal{I}} & m_{mr}\boldsymbol{\mathcal{I}} & m_b\boldsymbol{\mathcal{I}} \\ \mathbf{D}_f + \tilde{m}\tilde{\mathbf{r}} & \mathbf{I} - m_{rb}\hat{\mathbf{r}}_{rb}\hat{\mathbf{r}}_{rb} - m_{mr}\hat{\mathbf{r}}_{mr}\hat{\mathbf{r}}_{mr} - m_b\hat{\mathbf{r}}_b\hat{\mathbf{r}}_{rb} & m_{rb}\hat{\mathbf{r}}_{mr} & m_{mr}\hat{\mathbf{r}}_{mr} & m_b\hat{\mathbf{r}}_b \\ m_{rb}\boldsymbol{\mathcal{I}} & -m_{rb}\hat{\mathbf{r}}_{rb} & m_{rb}\boldsymbol{\mathcal{I}} & \mathbf{0} & \mathbf{0} \\ m_{mr}\boldsymbol{\mathcal{I}} & -m_{mr}\hat{\mathbf{r}}_{mr} & \mathbf{0} & m_{mr}\boldsymbol{\mathcal{I}} & \mathbf{0} \\ m_b\boldsymbol{\mathcal{I}} & -m_b\hat{\mathbf{r}}_b & \mathbf{0} & \mathbf{0} & m_b\boldsymbol{\mathcal{I}} \end{bmatrix}$$

where $\mathbf{I} = \mathbf{I}_{rb} + \mathbf{I}_{mr} + \mathbf{I}_b + \mathbf{I}_f$, $\tilde{m}\tilde{\mathbf{r}} = m_{rb}\hat{\mathbf{r}}_{rb} + m_{mr}\hat{\mathbf{r}}_{mr} + m_b\hat{\mathbf{r}}_b$. The momentum and angular momentum of the particle system of the vehicle can be calculated by the derivative of T with respect to time, as shown in Equation (20).

$$\begin{aligned} \mathbf{P} = \frac{\partial T}{\partial \mathbf{V}} &= \mathbf{M}_f\mathbf{V} + m_{mr}(\mathbf{V} + \hat{\mathbf{\Omega}}\mathbf{r}_{mr} + \dot{\mathbf{r}}_{mr}) + m_b(\mathbf{V} + \hat{\mathbf{\Omega}}\mathbf{r}_b + \dot{\mathbf{r}}_b) \\ &\quad + m_{rb}(\mathbf{V} + \hat{\mathbf{\Omega}}\mathbf{r}_{rb} + \dot{\mathbf{r}}_{rb}) \\ \mathbf{\Pi} = \frac{\partial T}{\partial \mathbf{\Omega}} &= (\mathbf{I}_{rb} + \mathbf{I}_{mr} + \mathbf{I}_b + \mathbf{I}_f)\mathbf{\Omega} + m_{mr}\hat{\mathbf{r}}_{mr}(\mathbf{V} + \hat{\mathbf{\Omega}}\mathbf{r}_{mr} + \dot{\mathbf{r}}_{mr}) \\ &\quad + m_b\hat{\mathbf{r}}_b(\mathbf{V} + \hat{\mathbf{\Omega}}\mathbf{r}_b + \dot{\mathbf{r}}_b) + m_{rb}\hat{\mathbf{r}}_{rb}(\mathbf{V} + \hat{\mathbf{\Omega}}\mathbf{r}_{rb} + \dot{\mathbf{r}}_{rb}) \end{aligned} \tag{20}$$

Rewriting Equation (20) into the expressions of $\mathbf{V}$ and $\mathbf{\Omega}$, Equation (21) can be obtained.

$$\begin{bmatrix} \mathbf{V} \\ \mathbf{\Omega} \end{bmatrix} = \aleph_1^{-1}\begin{bmatrix} \mathbf{P} \\ \mathbf{\Pi} \end{bmatrix} - \aleph_1^{-1}\aleph_2\begin{bmatrix} \dot{\mathbf{r}}_{rb} \\ \dot{\mathbf{r}}_{mr} \\ \dot{\mathbf{r}}_b \end{bmatrix} \tag{21}$$

where:

$$\aleph_1 = \begin{bmatrix} \mathbf{M}_f + (m_{rb} + m_{mr} + m_b)\boldsymbol{\mathcal{I}} & -m_{rb}\hat{\mathbf{r}}_{rb} - m_{mr}\hat{\mathbf{r}}_{mr} - m_b\hat{\mathbf{r}}_b \\ m_{rb}\hat{\mathbf{r}}_{rb} + m_{mr}\hat{\mathbf{r}}_{mr} + m_b\hat{\mathbf{r}}_b & \mathbf{I} - m_{rb}\hat{\mathbf{r}}_{rb}\hat{\mathbf{r}}_{rb} - m_{mr}\hat{\mathbf{r}}_{mr}\hat{\mathbf{r}}_{mr} - m_b\hat{\mathbf{r}}_b\hat{\mathbf{r}}_{rb} \end{bmatrix}$$

$$\aleph_2 = \begin{bmatrix} m_{rb}\boldsymbol{\mathcal{I}} & m_{mr}\boldsymbol{\mathcal{I}} & m_b\boldsymbol{\mathcal{I}} \\ m_{rb}\hat{\mathbf{r}}_{mr} & m_{mr}\hat{\mathbf{r}}_{mr} & m_b\hat{\mathbf{r}}_b \end{bmatrix}$$

Ignoring the weak coupling term, the state equation of the vehicle can be represented as shown in Equation (22), by taking the derivative with respect to time on both sides of Equation (21).

$$\begin{bmatrix} \dot{\mathbf{V}} \\ \dot{\mathbf{\Omega}} \end{bmatrix} = \aleph_1^{-1}\begin{bmatrix} \dot{\mathbf{P}} \\ \dot{\mathbf{\Pi}} \end{bmatrix} - \aleph_1^{-1}\aleph_2\begin{bmatrix} \ddot{\gamma}\mathbf{e}_1 \\ \ddot{\mathbf{r}}_{mr} \end{bmatrix} \tag{22}$$

2.4. Hydrodynamic Forces

The non-viscous hydrodynamic coefficients of the vehicle are mainly caused by the acceleration of the motion of the vehicle, which are inertial hydrodynamic coefficients and can be represented by an additional mass matrix. The design of an underwater unmanned vehicle generally has two symmetry planes, the upper and lower symmetry planes $\mathbf{e_1} - \mathbf{e_2}$, and the left and right symmetry planes $\mathbf{e_1} - \mathbf{e_3}$. In order to further simplify the motion model, it is assumed that the DUV studied in this paper has a front and rear symmetrical design which means the vehicle is symmetric about the $\mathbf{e_2} - \mathbf{e_3}$ plane. Therefore, the three sub-matrices

in the mass matrix can be simplified to the form of Equation (23). The parameters on the main diagonal of the matrix are retained, while the rest of the parameters are zero.

$$\begin{aligned} \mathbf{M}_f &= [M_{f1}, M_{f2}, M_{f3}]\boldsymbol{\mathcal{I}} \\ \mathbf{I}_f &= [I_{f1}, I_{f2}, I_{f3}]\boldsymbol{\mathcal{I}} \\ \mathbf{D}_f &= \mathbf{0} \end{aligned} \tag{23}$$

The viscous hydrodynamic force is mainly related to the speed of the vehicle and the external control surface, including drag D; drift force SF; vertical force L; and moments T_1, T_2 and T_3. The hydrodynamic force and moment of the vehicle in the vehicle frame can be calculated by Equations (24) and (25) with the simple hydrodynamic model.

$$\mathbf{F} = \mathbf{R}_{B\pi}^{\mathrm{T}} \begin{bmatrix} -X \\ Y \\ -Z \end{bmatrix} = \mathbf{R}_{B\pi}^{\mathrm{T}} \begin{bmatrix} -D \\ SF \\ -L \end{bmatrix} = \mathbf{R}_{B\pi}^{\mathrm{T}} \begin{bmatrix} -(K_{D0} + K_D\alpha^2)V^2 \\ K_\beta \beta V^2 \\ -(K_L\alpha)V^2 \end{bmatrix} \tag{24}$$

$$\mathbf{T} = \mathbf{R}_{B\pi}^{\mathrm{T}} \begin{bmatrix} K \\ M \\ N \end{bmatrix} = \mathbf{R}_{B\pi}^{\mathrm{T}} \begin{bmatrix} T_1 \\ T_2 \\ T_3 \end{bmatrix} = \mathbf{R}_{B\pi}^{\mathrm{T}} \begin{bmatrix} (K_{MR}\beta + K_p p)V^2 \\ (K_{M0} + K_M\alpha + K_q q)V^2 \\ (K_{MY}\beta + K_r r)V^2 \end{bmatrix} \tag{25}$$

where the constant term K_{D0}, K_D, K_β, K_{L0}, K_L, K_{MR}, K_p, K_{M0}, K_M, K_q, K_{MY} and K_r are the corresponding hydrodynamic coefficients, respectively.

3. Nonlinear MIMO Adaptive Backstepping Control

3.1. Assumptions

To simplify the problem, some simplifications of the dynamic model were made for the controller design and simulations. These simplifications were as follows:

1. The dynamic model of the vehicle was established in still water without disturbance caused by environment;
2. The DUV had three planes of symmetry;
3. The weak nonlinear terms and higher-order coupling terms in the dynamic model of DUV were neglected.

3.2. Controller Design

DUV is a nonlinear system with multiple inputs and multiple outputs, so it is quite difficult to precisely control. In this section, based on Lyapunov stability, a MIMO controller is designed for nonlinear control system and dual motion modes to realize dual-motion simulation of DUV. The state variables and control variables in a six-degrees-of-freedom equation of the vehicle are rewritten as Equations (26) and (27).

$$\begin{pmatrix} x_1 \\ x_2 \\ x_3 \\ x_4 \\ x_5 \\ x_6 \end{pmatrix} = \begin{pmatrix} \phi \\ \theta \\ \psi \\ u \\ v \\ w \end{pmatrix}, \begin{pmatrix} x_7 \\ x_8 \\ x_9 \\ x_{10} \\ x_{11} \\ x_{12} \end{pmatrix} = \begin{pmatrix} p \\ q \\ r \\ r_{mrx} \\ \gamma \\ m_b \end{pmatrix} \tag{26}$$

$$\boldsymbol{u}_c = \begin{pmatrix} u_1 \\ u_2 \\ u_3 \end{pmatrix} = \begin{pmatrix} \dot{r}_{mrx} \\ \dot{\gamma} \\ \dot{m}_b \end{pmatrix}, \boldsymbol{y}_d = \begin{pmatrix} \theta \\ \psi \\ u \end{pmatrix} = \begin{pmatrix} x_2 \\ x_3 \\ x_4 \end{pmatrix} \tag{27}$$

where $\boldsymbol{u}_c$ is the control input of the system, and $\boldsymbol{y}_d$ is the target control parameter of the vehicle system. The key variables of the vehicle during the operation process, including pitch angle θ, the heading angle ψ and the gliding speed u, are selected as the control objectives. The vehicle system can be adjusted to the target motion state by the three target

control objectives. Generally, it is assumed that the center of gravity of the remaining fixed mass of the vehicle coincides with the center of buoyancy in the process of controller design, which greatly simplifies the motion model. In this paper, the relationship between the center of gravity of the remaining fixed mass and the center of gravity of the moving mass needs to be considered. Therefore, the simplification of the motion control equations is more complex than the general system, and the difficulty of controller design is also increased. Simplified equations of motion, as shown in Equation (28) to Equation (39), are obtained by simplifying the six-degrees-of-freedom Equation (22) with the assumptions shown in Section 3.1. The moments generated by the moving mass m_{mr} and generated by the remaining fixed mass m_{rb} are equal.

$$\dot{x}_1 = x_7 + x_8 \sin x_1 \tan x_2 + x_9 \cos x_1 \tan x_2 \tag{28}$$

$$\dot{x}_2 = x_8 \cos x_1 - x_9 \sin x_1 \tag{29}$$

$$\dot{x}_3 = x_8 \sin x_1 \sec x_2 + x_9 \cos x_1 \sec x_2 \tag{30}$$

$$\dot{x}_4 = \frac{1}{M_{f1}}\left[-K_{D0}{x_4}^2 - x_{12} g \sin x_2\right] \tag{31}$$

$$\dot{x}_5 = \frac{1}{M_{f2}}\left[(K_\beta - K_{D0})x_4 x_5 + x_{12} g \sin x_1 \cos x_2 - x_9 x_4 (x_{12} + m_{mr} + m_{rb} + M_{f1})\right] \tag{32}$$

$$\dot{x}_6 = \frac{1}{M_{f3}}[-(K_L + K_{D0})x_4 x_6 + x_{12} g \cos x_1 \cos x_2] \tag{33}$$

$$\dot{x}_7 = \frac{1}{I_{f1}}\begin{bmatrix} K_{MR} x_4 x_5 + K_p x_7 {x_4}^2 - g \cos x_2 \sin x_1 m_{rb} r_{rb3} \\ -m_{mr} R_{mr} g \cos x_2 (\cos x_1 \sin x_{11} + \sin x_1 \cos x_{11}) \end{bmatrix} \tag{34}$$

$$\dot{x}_8 = \frac{1}{I_{f2}}\begin{bmatrix} x_4 x_6 \left(M_{f3} - M_{f1} + K_M\right) - x_{12} r_{b1} g \cos x_1 \cos x_2 + K_q x_8 {x_4}^2 \\ -m_{mr} g (x_{10} \cos x_1 \cos x_2 + R_{mr} \sin x_2 \cos x_{11}) \\ -g m_{rb} (\cos x_2 \cos x_1 r_{rb1} + \sin x_2 r_{rb3}) \end{bmatrix} \tag{35}$$

$$\dot{x}_9 = \frac{1}{I_{f3}}\begin{bmatrix} x_4 x_5 \left(M_{f1} - M_{f2} + K_{MY}\right) + x_{12} r_{b1} g \sin x_1 \cos x_2 + K_r x_9 {x_4}^2 \\ +m_{mr} g (x_{10} \sin x_1 \cos x_2 - R_{mr} \sin x_2 \sin x_{11}) + g \cos x_2 \sin x_1 m_{rb} r_{rb1} \end{bmatrix} \tag{36}$$

$$\dot{x}_{10} = u_1 \tag{37}$$

$$\dot{x}_{11} = u_2 \tag{38}$$

$$\dot{x}_{12} = u_3 \tag{39}$$

To overcome the aforementioned difficulties in multimode control, an adaptive backstepping controller is presented in this section. Adaptive backstepping control is widely used in current nonlinear systems, however, establishing the proper Lyapunov function is also extremely challenging. The control laws of the MIMO system are designed as Equations (40) and (41).

$$\begin{bmatrix} u_1 \\ u_2 \end{bmatrix} = \begin{bmatrix} \mathbf{A}_1 & \mathbf{A}_2 \end{bmatrix}^{-1} \begin{bmatrix} \frac{U_1 I_{f2} I_{f3}}{m_{mr} g} \\ \frac{U_2 I_{f2} I_{f3}}{m_{mr} g} \end{bmatrix} \tag{40}$$

$$\mathbf{A}_1 = \begin{bmatrix} \cos^2 x_1 \cos x_2 I_{f3} + \sin^2 x_1 \cos x_2 I_{f2} \\ \sin x_1 \cos x_1 I_{f3} - \cos x_1 \sin x_1 I_{f2} \end{bmatrix}$$

$$\mathbf{A}_2 = \begin{bmatrix} -\left(R_{mr} \cos x_1 \sin x_2 \sin x_{11} I_{f3} + R_{mr} \sin x_1 \sin x_2 \cos x_{11} I_{f2}\right) \\ -(R_{mr} \sin x_1 \tan x_2 \sin x_{11} I_{f3} - R_{mr} \cos x_1 \tan x_2 \cos x_{11} I_{f2}) \end{bmatrix}$$

$$u_3 = \frac{M_{f1}[c_4(z_{12} - c_4 z_4) + c_{12} z_{12}] - 2K_{D0} \dot{x}_4 x_4 - \dot{x}_2 x_{12} g \cos x_2}{g \sin x_2} \tag{41}$$

where the A_1, A_2, U_1 and U_2 will be shown in following parts.

Theorem 1. *Depending on the nonlinear system shown in Equations (28)–(39), choose control laws given by Equations (40) and (41); the tracking error of statespace vector converges to zero asymptotically for any initial position.*

Proof of Theorem 1. The MIMO ABC controller will be designed through the following steps.

Step 1. Define

$$z_1 = x_1 - \mu_1 \tag{42}$$
$$z_5 = x_5 - \mu_2 \tag{43}$$
$$z_6 = x_6 - \mu_3 \tag{44}$$
$$z_7 = x_7 - \mu_4 \tag{45}$$
$$z_8 = x_8 - \mu_5 \tag{46}$$
$$z_9 = x_9 - \mu_6 \tag{47}$$
$$z_{10} = x_{10} - \mu_7 \tag{48}$$
$$z_{11} = x_{11} - \mu_8 \tag{49}$$
$$z_{12} = x_{12} - \mu_9 \tag{50}$$
$$z_2 = x_2 - y_{1d} \tag{51}$$
$$z_3 = x_3 - y_{2d} \tag{52}$$
$$z_4 = x_4 - y_{3d} \tag{53}$$

where μ_i is the estimated value of the state parameter. z_i is the difference value between the current state parameter and the estimated value. The positive definite Lyapunov function of the system can be constructed as Equation (54).

$$V = \sum_{i=1}^{12} \frac{1}{2} {z_i}^2 \tag{54}$$

Take the derivative of both sides of Equation (54) and make the derivative negative definite to obtain the expression shown in Equation (55).

$$\dot{V} = \sum_{i=1}^{12} z_i \dot{z}_i \leqslant 0 \tag{55}$$

Step 2. Considering Equation (31), let $\dot{z}_4 = \dot{x}_4 - \dot{y}_{3d} = z_{12} - c_4 z_4$, where c_i is a constant. With this, we can obtain:

$$z_{12} = \frac{1}{M_{f1}} \left[-K_{D0} {x_4}^2 - x_{12} g \sin x_2 \right] + c_4 z_4 \tag{56}$$

The expression of $\dot{z}_{12}$ can be obtained by differentiating both sides of Equation (56), and let $\dot{z}_{12} = -c_{12} z_{12}$, so that the expression of the control input u_3 can be calculated, as shown in Equation (41).

Step 3. Considering Equation (29), let $\dot{z}_2 = \dot{x}_2 - \dot{y}_{1d} = z_8 - c_2 z_2$, and $\dot{z}_8$ can be calculated by differentiating with respect to z_8, as shown in Equation (57).

$$\dot{z}_8 = \dot{x}_8 \cos x_1 - \dot{x}_1 x_8 \sin x_1 - \dot{x}_9 \sin x_1 - \dot{x}_1 x_9 \cos x_1 + c_2 (z_8 - c_2 z_2) \tag{57}$$

The expression of z_{10} can be obtained by assuming $\dot{z}_8 = z_{10} - c_8 z_8$. The quadratic linear equation shown in Equation (58) about u_1, u_2 can be obtained by differentiating with respect to z_{10} and assume $\dot{z}_{10} = -c_{10} z_{10}$.

$$U_1 = \begin{bmatrix} \dfrac{\cos x_1}{I_{f2}} m_{mr} g(u_1 \cos x_1 \cos x_2 - u_2 R_{mr} \sin x_2 \sin x_{11}) \\ + \dfrac{\sin x_1}{I_{f3}} m_{mr} g(u_1 \sin x_1 \cos x_2 - u_2 R_{mr} \sin x_2 \cos x_{11}) \end{bmatrix} \tag{58}$$

where:

$$U_1 = U_{11} + U_{12} + U_{13} + U_{14} + U_{15} + U_{16} + U_{17}$$

$$U_{11} = \frac{-\dot{x}_1 \sin x_1}{I_{f2}} \begin{bmatrix} x_4 x_6 \left(M_{f3} - M_{f1} + K_M \right) - x_{12} r_{b1} g \cos x_1 \cos x_2 \\ -m_{mr} g(x_{10} \cos x_1 \cos x_2 + R_{mr} \sin x_2 \cos x_{11}) + K_{M0} {x_4}^2 + K_q x_8 {x_4}^2 \end{bmatrix}$$

$$U_{12} = \frac{\cos x_1}{I_{f2}} \begin{bmatrix} (\dot{x}_4 x_6 + x_4 \dot{x}_6) \left(M_{f3} - M_{f1} + K_M \right) - u_3 r_{b1} g \cos x_1 \cos x_2 \\ -m_{mr} g(-\dot{x}_1 x_{10} \sin x_1 \cos x_2 - \dot{x}_2 x_{10} \cos x_1 \sin x_2 + \dot{x}_2 R_{mr} \cos x_2 \cos x_{11}) \\ + \dot{x}_1 x_{12} r_{b1} g \sin x_1 \cos x_2 + \dot{x}_2 x_{12} r_{b1} g \cos x_1 \sin x_2 \\ + K_q \dot{x}_8 {x_4}^2 + 2 K_q \dot{x}_4 x_8 x_4 \end{bmatrix}$$

$$U_{13} = \frac{-\dot{x}_1 \cos x_1}{I_{f3}} \begin{bmatrix} x_4 x_5 \left(M_{f1} - M_{f2} + K_{MY} \right) + x_{12} r_{b1} g \sin x_1 \cos x_2 \\ + m_{mr} g(x_{10} \sin x_1 \cos x_2 - R_{mr} \sin x_2 \sin x_{11}) + K_r x_9 {x_4}^2 \end{bmatrix}$$

$$U_{14} = -\frac{\sin x_1}{I_{f3}} \begin{bmatrix} (\dot{x}_4 x_5 + x_4 \dot{x}_5) \left(M_{f1} - M_{f2} + K_{MY} \right) + u_3 r_{b1} g \sin x_1 \cos x_2 \\ + \dot{x}_1 x_{12} r_{b1} g \cos x_1 \cos x_2 - \dot{x}_2 x_{12} r_{b1} g \sin x_1 \sin x_2 \\ + m_{mr} g(\dot{x}_1 x_{10} \cos x_1 \cos x_2 - \dot{x}_2 x_{10} \sin x_1 \sin x_2 - \dot{x}_2 R_{mr} \cos x_2 \sin x_{11}) \\ + K_r \dot{x}_9 {x_4}^2 + 2 K_r \dot{x}_4 x_9 x_4 \end{bmatrix}$$

$$U_{15} = -(x_8 \sin x_1 + x_9 \cos x_1) \begin{pmatrix} \dot{x}_7 + \dot{x}_8 \sin x_1 \tan x_2 + \dot{x}_1 x_8 \cos x_1 \tan x_2 \\ + \dot{x}_2 x_8 \sin x_1 \sec^2 x_2 + \dot{x}_9 \cos x_1 \tan x_2 \\ - \dot{x}_1 x_9 \sin x_1 \tan x_2 + \dot{x}_2 x_9 \cos x_1 \sec^2 x_2 \end{pmatrix}$$

$$U_{16} = -\dot{x}_1 (\dot{x}_8 \sin x_1 + \dot{x}_1 x_8 \cos x_1 + \dot{x}_9 \cos x_1 - \dot{x}_1 x_9 \sin x_1)$$

$$U_{17} = c_2 (\dot{z}_8 - c_2 \dot{z}_2) + c_8 \dot{z}_8 + c_{10} z_{10}$$

Step 4. By using the same procedure, the Equation (59) can be obtained by the transformation and derivative of Equation (30).

$$z_9 = x_8 \sin x_1 \sec x_2 + x_9 \cos x_1 \sec x_2 + c_3 z_3 - \dot{y}_{2d} \tag{59}$$

where $\dot{y}_{2d}$ is the gradient of the heading angle. Assume $\dot{z}_9 = z_{11} - c_9 z_9$ and $\dot{z}_{11} = -c_{11} z_{11}$, then, the other binary system of first order equations of u_1 and u_2 can be obtained, as shown in Equation (60)

$$U_2 = \begin{bmatrix} \dfrac{\sin x_1 \sec x_2}{I_{f2}} m_{mr} g(u_1 \cos x_1 \cos x_2 - u_2 R_{mr} \sin x_2 \sin x_{11}) \\ - \dfrac{\cos x_1 \sec x_2}{I_{f3}} m_{mr} g(u_1 \sin x_1 \cos x_2 - u_2 R_{mr} \sin x_2 \cos x_{11}) \end{bmatrix} \tag{60}$$

where:

$$
\begin{aligned}
U_2 &= U_{21} + U_{22} + U_{23} + U_{24} + U_{25} + U_{26} + U_{27} \\
U_{21} &= \dot{x}_8(\dot{x}_1 \cos x_1 \sec x_2 + \dot{x}_2 \sin x_1 \sec x_2 \tan x_2) \\
U_{22} &= \frac{\sin x_1 \sec x_2}{I_{f2}} \begin{bmatrix} (\dot{x}_4 x_6 + x_4 \dot{x}_6)\left(M_{f3} - M_{f1} + K_M\right) - u_3 r_{b1} g \cos x_1 \cos x_2 \\ +\dot{x}_1 x_{12} r_{b1} g \sin x_1 \cos x_2 + \dot{x}_2 x_{12} r_{b1} g \cos x_1 \sin x_2 \\ -m_{mr} g(-\dot{x}_1 x_{10} \sin x_1 \cos x_2 - \dot{x}_2 x_{10} \cos x_1 \sin x_2 \\ +\dot{x}_2 R_{mr} \cos x_2 \cos x_{11}) + K_q \dot{x}_8 {x_4}^2 + 2K_q \dot{x}_4 x_8 x_4 \end{bmatrix} \\
U_{23} &= \dot{x}_9(-\dot{x}_1 \sin x_1 \sec x_2 + \dot{x}_2 \cos x_1 \sec x_2 \tan x_2) \\
U_{24} &= \frac{\cos x_1 \sec x_2}{I_{f3}} \begin{bmatrix} (\dot{x}_4 x_5 + x_4 \dot{x}_5)\left(M_{f1} - M_{f2} + K_{MY}\right) + u_3 r_{b1} g \sin x_1 \cos x_2 \\ +\dot{x}_1 x_{12} r_{b1} g \cos x_1 \cos x_2 - \dot{x}_2 x_{12} r_{b1} g \sin x_1 \sin x_2 \\ +m_{mr} g(\dot{x}_1 x_{10} \cos x_1 \cos x_2 - \dot{x}_2 x_{10} \sin x_1 \sin x_2 \\ -\dot{x}_2 R_{mr} \cos x_2 \sin x_{11}) + K_r \dot{x}_9 {x_4}^2 + 2K_r \dot{x}_4 x_9 x_4 \end{bmatrix} \\
U_{25} &= \begin{pmatrix} \dot{x}_7 + \dot{x}_8 \sin x_1 \tan x_2 + \dot{x}_1 x_8 \cos x_1 \tan x_2 \\ +\dot{x}_2 x_8 \sin x_1 \sec^2 x_2 + \dot{x}_9 \cos x_1 \tan x_2 \\ -\dot{x}_1 x_9 \sin x_1 \tan x_2 + \dot{x}_2 x_9 \cos x_1 \sec^2 x_2 \end{pmatrix} (x_8 \cos x_1 \sec x_2 - x_9 \sin x_1 \sec x_2) \\
U_{26} &= \begin{pmatrix} x_7 + x_8 \sin x_1 \tan x_2 \\ +x_9 \cos x_1 \tan x_2 \end{pmatrix} \begin{pmatrix} \dot{x}_8 \cos x_1 \sec x_2 - \dot{x}_1 x_8 \sin x_1 \sec x_2 \\ +\dot{x}_2 x_8 \cos x_1 \sec x_2 \tan x_2 - \dot{x}_9 \sin x_1 \sec x_2 \\ -\dot{x}_1 x_9 \cos x_1 \sec x_2 - \dot{x}_2 x_9 \sin x_1 \sec x_2 \tan x_2 \end{pmatrix} \\
U_{27} &= \begin{bmatrix} c_3(\dot{z}_9 - c_3 \dot{z}_3) + c_9 \dot{z}_9 + (\dot{z}_8 - c_2 \dot{z}_2)(x_8 \sin x_1 + x_9 \cos x_1) \sec x_2 \tan x_2 \\ +(z_8 - c_2 z_2)(\dot{x}_8 \sin x_1 + \dot{x}_1 x_8 \cos x_1 + \dot{x}_9 \cos x_1 - \dot{x}_1 x_9 \sin x_1) \sec x_2 \tan x_2 \\ +\dot{x}_2(z_8 - c_2 z_2)(x_8 \sin x_1 + x_9 \cos x_1)\left(\sec x_2 \tan^2 x_2 + \sec^3 x_2\right) + c_{11} z_{11} \end{bmatrix}
\end{aligned}
$$

Step 5. The system of linear equations in two variables for u_1 and u_2 is obtained by combining the quadratic linear equations, Equations (58) and (60), while U_1 and U_2 are related to u_3. The expression of u_1 and u_2 can be obtained by solving this system of linear equations, as shown in Equation (40). □

From the analysis of the motion law of the vehicle, the lateral velocity, the vertical velocity, and the roll angular velocity of DUV are all very small, and the difference between the state parameter and the estimated value is tiny enough to be ignored. Therefore, $z_1 = z_5 = z_6 = z_7 = 0$ can be set and then the final Lyapunov function of the system can be obtained as shown in Equation (61).

$$V = \frac{1}{2} z_2^2 + \frac{1}{2} z_3^2 + \frac{1}{2} z_8^2 + \frac{1}{2} z_9^2 + \frac{1}{2} z_4^2 + \frac{1}{2} z_{10}^2 + \frac{1}{2} z_{11}^2 + \frac{1}{2} z_{12}^2 \tag{61}$$

Theorem 2. *By choosing proper coefficients c_i, the glider system reaches global asymptotic stability.*

Proof of Theorem 2. The derivative form of the Lyapunov function is obtained by taking the first-order partial derivative of t on both sides of Equation (61), as shown in Equation (62).

$$
\begin{aligned}
\dot{V} &= z_2 \dot{z}_2 + z_3 \dot{z}_3 + z_8 \dot{z}_8 + z_9 \dot{z}_9 + z_4 \dot{z}_4 + z_{10} \dot{z}_{10} + z_{11} \dot{z}_{11} + z_{12} \dot{z}_{12} \\
&= -c_2 z_2^2 + z_2 z_8 - c_8 z_8^2 + z_8 z_{10} - c_{10} z_{10}^2 - c_3 z_3^2 + z_3 z_9 - c_9 z_9^2 \\
&\quad + z_9 z_{11} - c_{11} z_{11}^2 - c_4 z_4^2 + z_4 z_{12} - c_{12} z_{12}^2 \\
&\leqslant (0.5 - c_2) z_2^2 + (1 - c_8) z_8^2 + (0.5 - c_{10}) z_{10}^2 + (0.5 - c_3) z_3^2 + (1 - c_9) z_9^2 \\
&\quad + (0.5 - c_{11}) z_{11}^2 + (0.5 - c_4) z_4^2 + (0.5 - c_{12}) z_{12}^2
\end{aligned} \tag{62}
$$

It is obvious that if the proper coefficients $c_i \geq 0.5$ ($i = 2, 3, 4, 10, 11, 12$), $c_i \geq 1$ ($i = 8, 9$) are chosen, the value of Equation (62) is capable of remaining nonpositive. According to Lyapunov stability theory, the dynamic system reaches global asymptotic stability. □

4. Characteristics and Analysis of Dual-Modal Motion

The mutual switching between the two working modes of Argo and Glider is the key idea of deep-sea DUV. In this section, the switching process of the two working modes and the dual motion of the vehicle are simulated to analyze the changes in state parameters of DUV. Considering the actual application of DUV, the vehicle can switch the working mode at any depth to achieve the mission goal and meet the needs of multi-mode observation. The typical working mode of DUV is simulated and analyzed according to the following processes. DUV initially uses the Argo mode to descend. When it dives to a certain depth, it switches to the Glider mode for gliding motion. Then, it turns to the specified heading angle for a stably sawtooth gliding motion until it dives to the target depth and then goes up. When it goes up to the specified depth, it switches to Argo mode and continues to go up until it reaches the water surface. The parameters values of DUV used in the simulations are shown in Table A1.

$$
\begin{aligned}
V_d &= \begin{cases} 0.4\ \mathrm{m/s} & (t < 7000\ \mathrm{s}) \\ -0.6\ \mathrm{m/s} & (t \geqslant 7000\ \mathrm{s}) \end{cases} \\
\xi_d &= \begin{cases} -90^\circ & (t < 300\ \mathrm{s}) \\ -45^\circ & (t < 2000\ \mathrm{s}) \\ -45^\circ & (t < 5000\ \mathrm{s}) \\ 45^\circ & (t < 7000\ \mathrm{s}) \\ 90^\circ & (t \geqslant 7000\ \mathrm{s}) \end{cases} \\
\psi_d &= \begin{cases} 0\ \mathrm{rad} & (t < 300\ \mathrm{s}) \\ 0.002t\ \mathrm{rad} & (t < 2000\ \mathrm{s}) \\ 3.2\ \mathrm{rad} & (t < 7000\ \mathrm{s}) \\ 0\ \mathrm{rad} & (t \geqslant 7000\ \mathrm{s}) \end{cases}
\end{aligned}
\tag{63}
$$

The target trajectory of DUV motion is shown as Equation (63) (defined: the heading angle is zero when the DUV's attitude is vertically downward). The motion trajectory of DUV during the entire simulation process is shown in Figure 4. DUV starts to dive vertically with the working mode of Argo at the speed of 0.4 m/s. When the dive time reaches 300 s (the depth is about 100 m), it switches to the Glider mode and the pitch angle is switched to -45°. DUV transforms into a spiral shape movement and gradually turns to the target heading angle of 3.2 rad. After reaching the target heading angle (the time is about 2000 s), the sawtooth gliding motion is performed. When reaching the maximum diving time of 5000 s (the depth is about 1500 m), DUV switches to the upward attitude, and continues to ascend; pitch angle is adjusted to 45°. When the time is 7000 s (the depth is about 1000 m), it switches to the vertical attitude of the Argo mode and ascends to the water surface at a speed of 0.6 m/s. The change curves of state parameters of DUV during the movement are shown in Figure 5. In the process of simulation, the vertical state of DUV is redefined. Currently, the heading angle of DUV is zero, the position of the eccentric mass is $r_{mrx} = 0.75$ m, and the rotation angle is $\gamma = 180^\circ$.

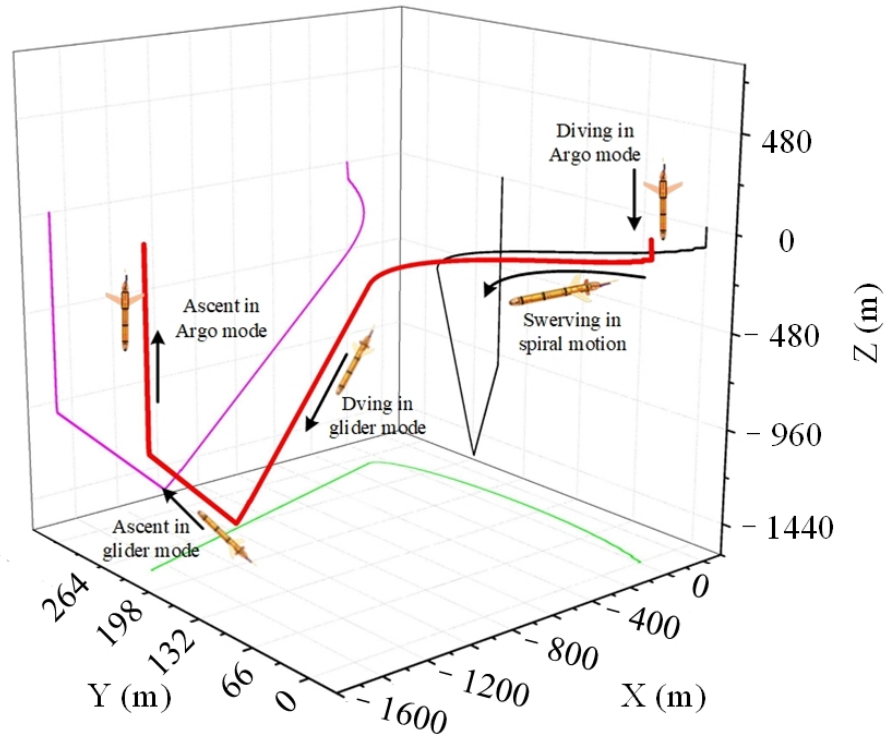


Figure 4. Dual-modal motion trajectory.

The controlling regulation can be expressed from the control input curve in Figure 5. It can be concluded from the changes in state parameters in Figure 6 that there is obvious vibration during the process of transforming from Argo mode to spiral motion mode. This is because the influence of the eccentric mass on the heading angle is indirect and the control effect is limited, and it is a slow process from the adjustment of the slider to the stabilization of the vehicle. Therefore, there is a large jitter. However, this jitter has little effect on the running trajectory of DUV. In general, during the entire dual motion simulation of DUV, each control variable can quickly converge to the target value. The control process is relatively stable. The motion trajectory of the vehicle has no obvious jitter phenomenon. The simulation results show that the attitude switching of deep-sea DUV in dual motion can be well controlled by the MIMO controller, which provides theoretical support for analyzing the motion and control laws of deep-sea DUV.

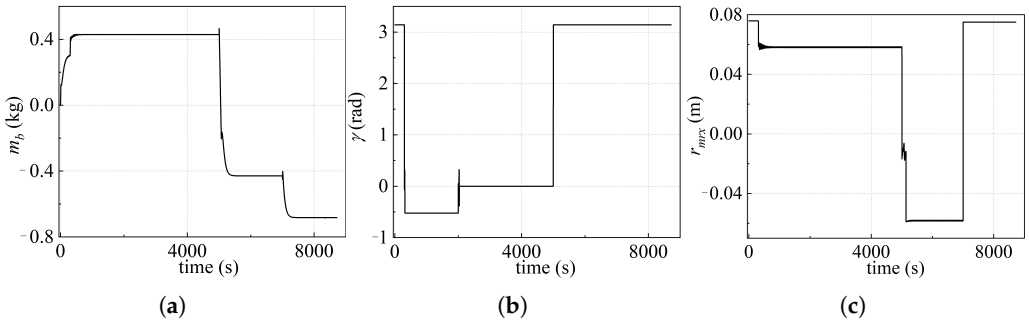


Figure 5. Control inputs for dual-modal simulation processes. (**a**) m_b, (**b**) γ, (**c**) r_{mrx}.

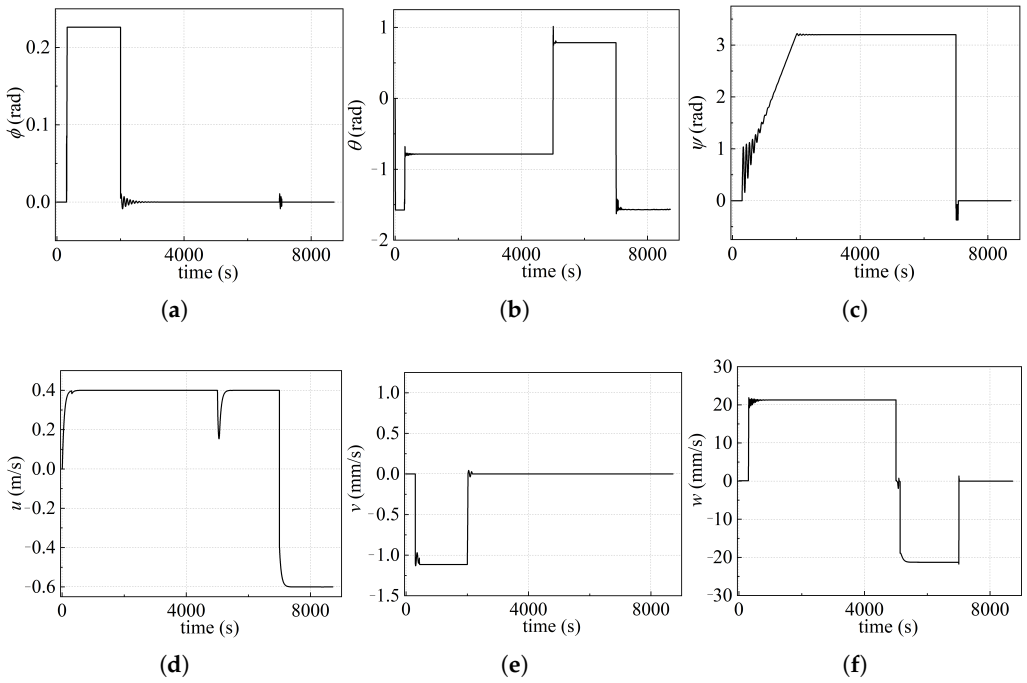


Figure 6. Variation curve of state parameters during multi-modal motion. (**a**) ϕ. (**b**) θ, (**c**) ψ, (**d**) u, (**e**) v, (**f**) w.

5. Sea Trials and Results

5.1. The Sea Test of the DUV in Single Mode

5.1.1. Course-Keeping Test of the DUV in Glider Mode

Directional navigation performance is a significant performance of DUV during the mission execution. It reflects the quality of the attitude control of the vehicle, and directly determines the strength of navigation ability. The navigation performance of the platform is tested and verified by conducting directional navigation and diving tests at constant speed. Figure 7 shows the gliding mission data of the vehicle at a pitch angle of 20°, a diving depth of 1000 m, and a speed of not less than 0.1 m/s.

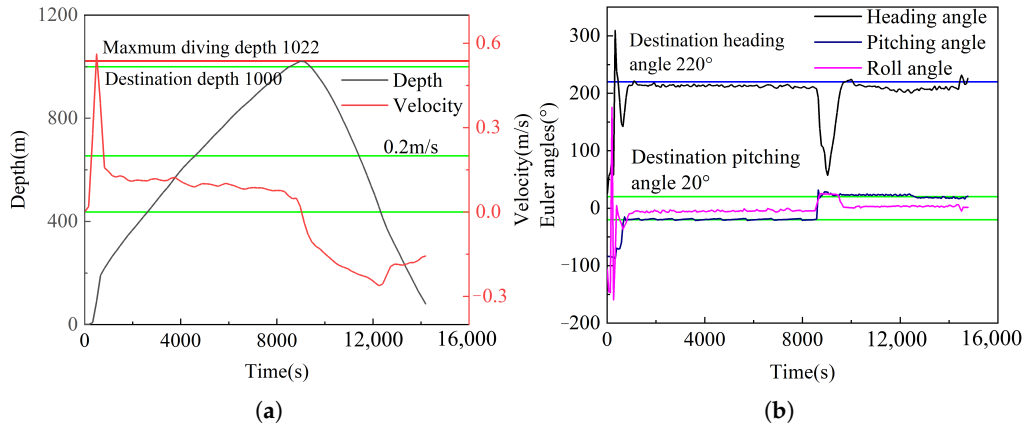


Figure 7. The frames of the dynamic model. (**a**) Depth and velocity, (**b**) Euler angles.

In order to ensure the sufficient height of the vehicle antenna above the water surface, the communication attitude of the vehicle is vertically downward when the vehicle is on the water surface. Currently, the vehicle is in the Argo mode. Figure 7b shows that the pitch angle of the vehicle is about 90° at the beginning of mission. After receiving the mission command on the surface, the vehicle starts to descend. When the depth exceeds 10 m,

the moveable mass of the attitude system starts to rotate and move to adjust the attitude of the vehicle. Then, the working mode of the vehicle is switched from the vertical attitude to the Glider gliding attitude with pitch and roll angles. At this time, the vehicle starts to glide and the pitch angle of the vehicle gradually changes from 90° to the target's pitch angle of 20°, and the heading angle gradually tends to the target heading angle. When the vehicle dives to 1000 m, the vehicle gradually floats up by adjusting the attitude system and buoyancy system to change the attitude and buoyancy of the vehicle. During the entire directional navigation mission, the pitch angle and navigation angle are well-controlled, both of which can reach the target angle. Through the control input of the experiment, shown in Figure 8, we also can obtain the same conclusions. As in conjunction with Figure 7, at the beginning of the mission, with the change in the moveable and rotatable mass, the attitude changed. The working mode of the DUV switched from Argo to Glider. Figure 8 also demonstrated the validity of the sub-driven system and the control method.

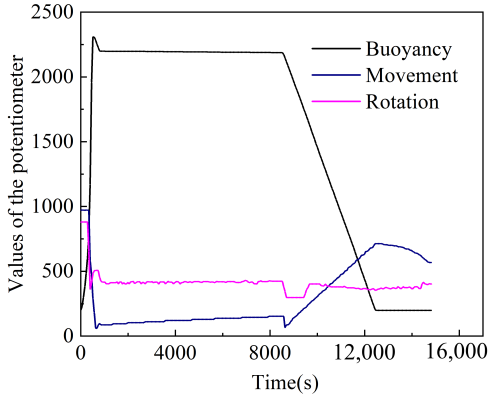


Figure 8. Control input of the DUV test in glider mode.

In contrast to the traditional Glider mode, DUV has a larger pitch angle and faster speed during the initial dive. This mode allows the vehicle to quickly pass through the turbulent zone to reach a stable area under the water surface (a depth of greater than 20 m). The entire gliding work-flow chart of DUV is shown in Figure 9. In the case of small ocean currents, it usually takes 4 to 6 h to complete the sawtooth profile with a horizontal distance of 3 to 6 km and a vertical distance of 600 to 1000 m.

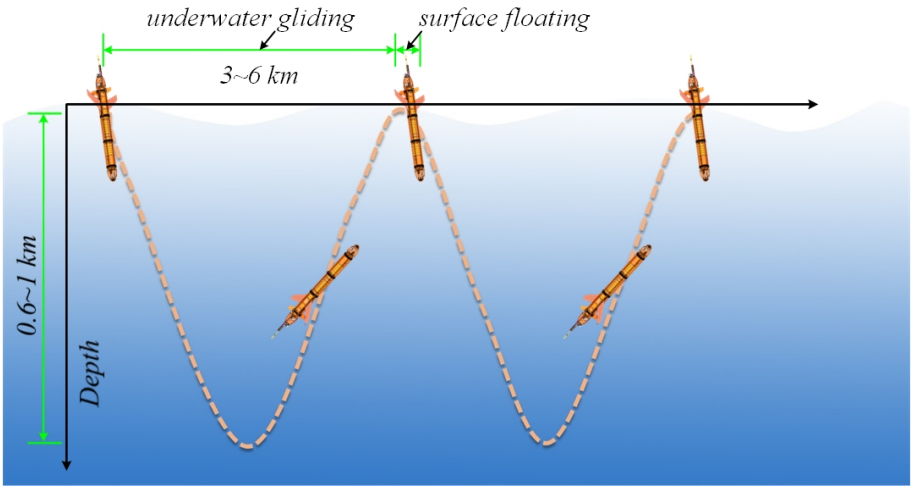


Figure 9. The frames of the dynamic model.

5.1.2. Diving Performance of the DUV in Argo Mode

The diving performance of Argo mode was evaluated in the South China Sea, including the depth tests of 3500 m and 3700 m. The depth and velocity curves are shown in Figure 10.

The vehicle dives through the buoyancy adjustment system absorbing oil on the water surface, then the vehicle gradually accelerates. While the density of the seawater gradually increases as the depth increases, the vehicle speed reaches the maximum and then starts to decelerate. The buoyancy system begins to pump oil to an outer oil pocket when the target depth is reached, and then the vehicle begins to ascend. It can be seen from the data that the overshoot of the maximum diving depth is within 200 m. This is due to the excessive driving buoyancy of the system during the test. When the vehicle dives to the target depth, the gravity is still greater than the buoyancy, and the buoyancy system still needs to pump oil outward to increase the buoyancy of the vehicle to reduce the diving speed.

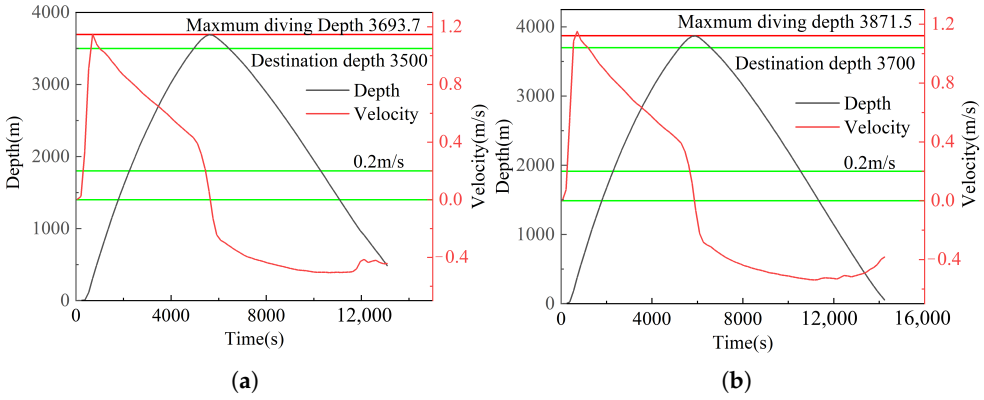


Figure 10. The frames of the dynamic model. (**a**) Depth and velocity curves of 3500 m, (**b**) depth and velocity curves of 3700 m.

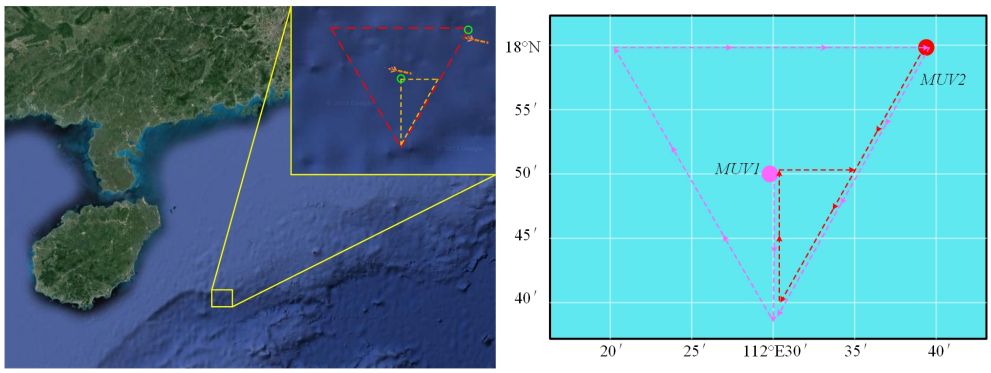
5.2. The Network Sea Test with Two DUVs

From 24 to 30 April 2021, Shanghai Jiao Tong University and Ocean University of China carried out a dual network sea trial of DUV in the South China Sea. Two DUVs were deployed successively to complete a large triangular path and a small triangular path to observe the temperature and salinity characteristics of the target area, as shown in Figure 11. During the sea trial, both DUVs were equipped with a Seabird 49 CTD sensor to collect the temperature and salinity parameters of the target area. The sampling frequency of CTD is 0.5 Hz. The detailed parameters of the DUV dual task are shown in Table 1. Two DUVs collected 55 data profiles, covering seawater depths of 600 m to 1000 m during a period of 7 days.

Table 1. The deployment and recovery time of DUVs.

Number	Deployment Time	Recovery Time	Average Depth	Profile Number
DUV1	24 April 2021 19:47:04	30 April 2021 12:30:44	1000 m	23
DUV2	25 April 2021 03:47:50	30 April 2021 11:32:30	600 m	32

Based on the temperature and salinity data collected by DUVs (the temperature and salinity data collected by DUVs are shown in Figure 12), a three-dimensional temperature field and salinity field was constructed using the spatio-temporal Kriging method [27,28]. As shown in Figure 12a,b, two argo missions at a depth of 1100 m were performed by DUV1 first, and then glider missions at a depth of 1000 m were executed. There are some differences in operating performances between the DUV1 and DUV2, which are caused by the diversities in mass distributions and payloads. As shown in Figure 12c,d, DUV2 performed two argo missions at a depth of 600 m and two argo missions at a depth of 1000 m first and then executed the glider missions.



(**a**) (**b**)

Figure 11. Introduction of sea trial. (**a**) Trial area in the South China Sea, (**b**) movement trajectories of DUVs.

The variogram is the basic tool of Kriging interpolation, and the spatial variogram equation is defined as Equation (64).

$$\xi(h) = Var[Z(x) - Z(x+h)] = \frac{1}{2}E[Z(x) - Z(x+h)]^2 \tag{64}$$

where the regionalization variable $Z(x) \in S$ is second-order stable, x is the position of the sampling point in the spatial domain, and h is the spatial distance. The space domain is represented by S and the time domain is represented by T so that the spatio-temporal variogram can be defined as Equation (65).

$$\xi(h_s, h_t) = Var[Z(s+h_s, t+h_t) - Z(s,t)] = \frac{1}{2}E[Z(s+h_s, t+h_t) - Z(s,t)]^2 \tag{65}$$

where the position of the sampling point in the space-time domain is represented as (s,t) and the spatial and temporal distances are represented as h_s and h_t, respectively.

In this section, the method of a statistical histogram is used to test the stability hypothesis of seawater temperature and salinity. The fitting method of weighted regression was selected to calculate the variation fitting function. Finally, the estimated variance was used to describe the accuracy of the Kriging estimator, as shown in Equation (66).

$$\sigma_E{}^2 = Var(R(x)) = Var(Z(x) - Z^*(x)) \tag{66}$$

where $Z(x)$ is the true value, $Z^*(x)$ is the estimated value, and $R(x)$ is the estimated error. In order to calculate the time variogram, this paper downloaded the temperature and salinity data of the corresponding area from the APDRC (Asia Pacific Data Research Center) developed by the University of Hawaii. Finally, our sea trial data was synchronized with the downloaded data to construct a three-dimensional ocean salinity field and temperature field.

This paper uses the experimental data on 26 April 2021 for its research. The three-dimensional salinity and temperature fields of our study area are shown in Figure 13. Figure 13a shows that the salinity changes greatly from the sea surface to 300 m, from about 3.8 S/m to 5.6 S/m, but remains basically stable below a 300 m depth. It can be, likewise, seen from Figure 13b that the temperature from the sea surface to 300 m varies greatly, from about 12 °C to 28 °C, but changes slowly below the 300 m water depth. Overall, the general trends of salinity and temperature changes in the studied sea area are reasonable.

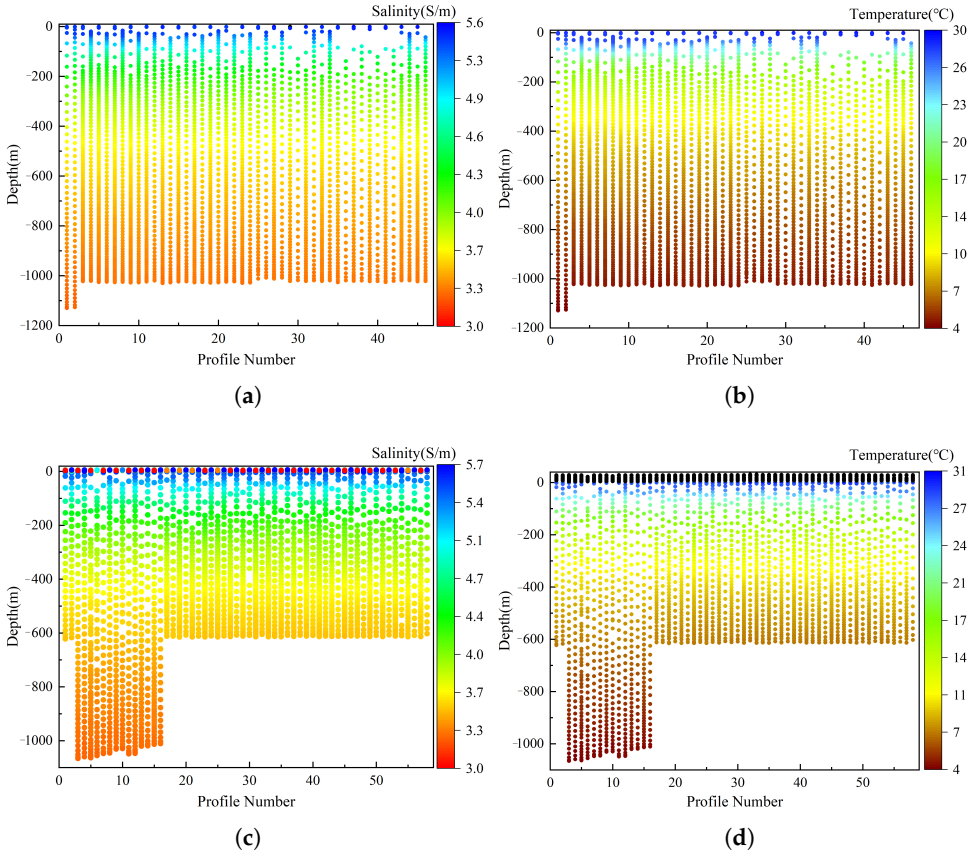


Figure 12. Part of the temperature and salinity data collected by DUV1 (top), DUV2 (bottom). (**a**) Salinity of DUV1, (**b**) temperature of DUV1, (**c**) salinity of DUV2, (**d**) temperature of DUV2.

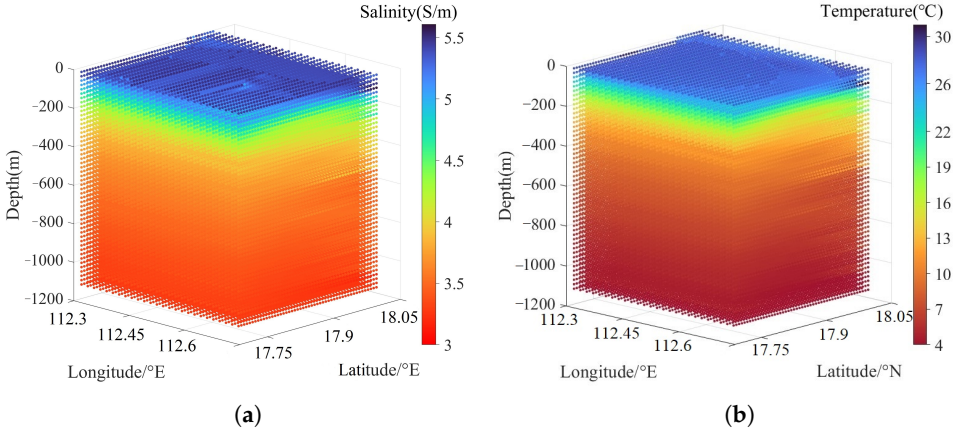
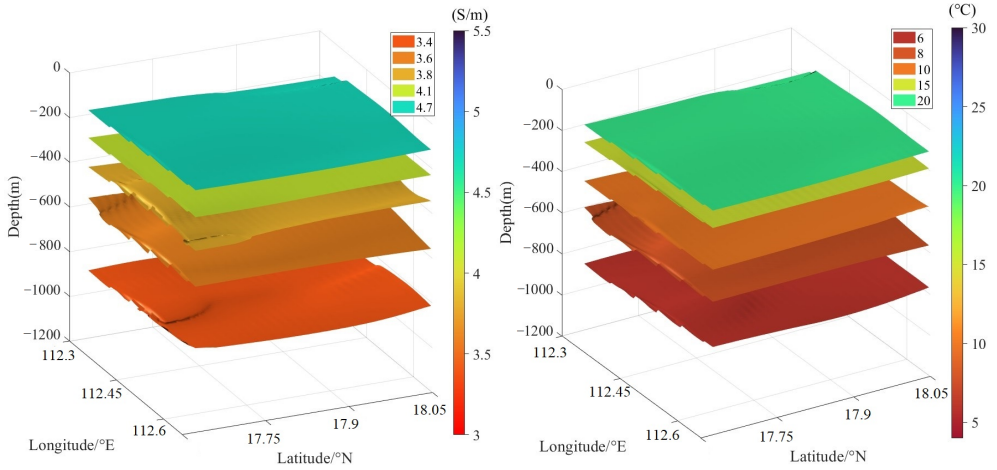


Figure 13. 3D salinity field and 3D temperature field. (**a**) Salinity, (**b**) temperature.

Feature isosurfaces can be used to reveal mesoscale or subscale ocean phenomena, and can also be used to track the movement of water masses in ocean circulation, which is of great significance to the ocean model. Isosurfaces for different salinity and temperature values are extracted from the three-dimensional salinity and three-dimension temperature fields, as shown in Figure 14. The extracted salinity isosurfaces are 3.4 S/m, 3.6 S/m, 3.8 S/m, 4.1 S/m and 4.7 S/m. The extracted isothermal surfaces are 6 °C, 8 °C, 10 °C, 15 °C and 20 °C. Figure 14 shows that the salinity and temperature gradually decrease from the surface layer to the deep layer. The overall change trend is consistent with the three-dimensional field, which can provided some references for analysing the structure of temperature and salinity in the ocean.



(**a**) (**b**)

Figure 14. Isosurfaces of salinity and temperature at different values. (**a**) Isosurfaces of salinity, (**b**) Isosurfaces of temperature.

6. Conclusions and Discussion

In this paper, a complete dynamic model was established to describe the dual operating motion based on the novel DUV observation platform and the Newton–Euler method, and a nonlinear MIMO adaptive inverse controller was proposed to control the dynamic system. The distance between the center of gravity and the center buoyancy was considered to precisely describe the operating process and resolve the issues caused by mode switching. The asymptotic stability of the dynamic system was verified by using the Lyapunov stability criterion. Then, combined with the experimental data acquired by two DUVs in the South China Sea in April 2021, the performance of the DUV and the proposed method were verified. The results show that the novel DUV has outstanding observational performance and is more suitable for multifarious and continuous oceanographic observation. In addition, the reconstruction of the three-dimensional ocean element field and the extraction of the temperature–salinity feature isosurfaces were initially carried out using the network test data and APDRC data. The data visualization results reflect the temperature and salinity structure of the target sea area.

The novel DUV and the adaptive controller proposed in this paper is to tackle the dual modal switching and observe the target ocean continuously and diversely. However, the proposed method is limited to the condition that the external environment is stable and the state of the model is clear. The disturbance of the external environment, the uncertainty parameters of the model, and the dynamic model of each actuator are not considered in this research. Actually, the movement of the actuators will have a great impact on the mode switching control and the uncertainties will cause errors in the sampling data, which affects the reconstruction of the three-dimension marine element field. Therefore, further research is needed for the next step.

Further work will focus on studying the motion control algorithm of DUV in practical situations and obtaining more accurate oceanographic observation data. However, the visualization of the three-dimensional oceanic element field, ocean feature surfaces and the real-time oceanic environment fields is also a research direction for the future.

Author Contributions: Conceptualization, B.Y.; methodology, C.L.; software, J.C.; formal analysis, J.C.; data curation, X.Z.; writing—original draft preparation, J.C.; writing—review and editing, R.L.; supervision, L.L. All authors have read and agreed to the published version of the manuscript.

Funding: This research was funded by Shanghai Sailing Program grant number 21YF1419900 and funded by the National Natural Science Foundation of China (NSFC) grant number 41527901.

Institutional Review Board Statement: Not applicable.

Informed Consent Statement: Informed consent was obtained from all subjects involved in the study. Written informed consent has been obtained from the patients to publish this paper.

Data Availability Statement: Not applicable.

Acknowledgments: We would like to express sincere thanks to associate researcher Xu Bo.

Conflicts of Interest: The authors declare no conflict of interest. The funders had no role in the design of the study; in the collection, analyses, or interpretation of data; in the writing of the manuscript, or in the decision to publish the results.

Abbreviations

The following abbreviations are used in this manuscript:

DUV	Dual-modal underwater vehicle
AUV	Autonomous underwater vehicle
MIMO	Multi-input and multi-output
ABC	Adaptive backstepping contorl
HUG	Hybrid underwater vehicle
APDRC	Asia Pacific Data Research Center

Appendix A

Table A1. The parameter values of DUV used in simulations.

Parameter	Value	Unit	Parameter	Value	Unit
m_{rb}	170.6	kg	m_{mr}	20	kg
r_{rb}	[0.052,0,0.0057]	m	I_{rb1}	3.25	$\mathrm{kg \cdot m^2}$
I_{rb2}	103.45	$\mathrm{kg \cdot m^2}$	I_{rb3}	104.06	$\mathrm{kg \cdot m^2}$
R_{mr}	0.028	m	r_{mrx}	$\in [-21, 17.1]$	mm
I^0_{mr}	diag[2.12,15.4,1.85]	$\mathrm{kg \cdot m^2}$	m_b	$\in [-1.5, 1.5]$	kg
$\mathbf{r}_b$	[0.015,0,00033]	m	m	190.6	kg
$Diameter$	0.301	m	$Length$	2.95	m
$\mathbf{M}_{f1}$	6.48	kg	$\mathbf{M}_{f2}$	95.58	kg
$\mathbf{M}_{f3}$	98.92	kg	$\mathbf{I}_{f1}$	3.55	$\mathrm{kg \cdot m^2}$
$\mathbf{I}_{f2}$	44.88	$\mathrm{kg \cdot m^2}$	$\mathbf{I}_{f3}$	40.18	$\mathrm{kg \cdot m^2}$
$N_{\dot{v}}$	8.57	$\mathrm{kg \cdot m}$	$Z_{\dot{q}}$	9.54	$\mathrm{kg \cdot m}$
K_{D0}	18.6	kg/m	K_D	380.29	$\mathrm{kg/(m \cdot rad^2)}$
K_{L0}	0	kg/m	K_L	330.99	$\mathrm{kg/(m \cdot rad^2)}$
K_β	−160.65	kg/(m·rad)	K_{MR}	−132.27	kg/rad
K_p	−42.23	$\mathrm{kg \cdot s/rad}$	K_{M0}	0	kg/rad
K_M	−116.74	kg/rad	K_q	−292.64	$\mathrm{kg \cdot s/rad^2}$
K_{MY}	96.1	kg/rad	K_r	−263.3	$\mathrm{kg \cdot s/rad}$

Table A2. The parameter values of DUV used in simulations.

Parameter	Explanation	Parameter	Explanation
$\mathbf{E_0}$	the origin of inertial frame	$\mathbf{i}, \mathbf{j}, \mathbf{k}$	the unit vectors of inertial frame
$\mathbf{B_0}$	the origin of body frame	$\mathbf{e_1}, \mathbf{e_2}, \mathbf{e_3}$	the unit vectors of body frame
$\boldsymbol{\pi_0}$	the origin of flow velocity frame	$\boldsymbol{\pi_1}, \boldsymbol{\pi_2}, \boldsymbol{\pi_3}$	the unit vectors of flow velocity frame
$\mathbf{b}$	the position of vehicle in inertial frame	x, y, z	the components of $\mathbf{b}$
$\boldsymbol{\theta}$	Euler angle in inertial frame	ϕ, θ, ψ	the components of $\boldsymbol{\theta}$
$\mathbf{V}$	the velocity of vehicle in body frame	u, v, w	the components of $\mathbf{V}$

Table A2. *Cont.*

Parameter	Explanation	Parameter	Explanation
$\mathbf{V_r}$	the velocity represented in body frame respected to current	v_{r1}, v_{r2}, v_{r3}	the components of $\mathbf{v_r}$
$\mathbf{\Omega}$	the angular velocity in body frame	p, q, r	the components of $\mathbf{\Omega}$
α	the attack angle	β	the drift angle
$\mathbf{R}_{EB}$	the rotation matrix from body frame to inertial frame	$\mathbf{R}_{\pi B}$	the rotation matrix from body frame to flow velocity frame
m	the total mass of DUV	m_{rb}, m_{mr}, m_b	the fixed mass, moving mass and variable mass of DUV
m_d	the constant displacement mass of the DUV	m_0	the net mass of the vehicle
$\mathbf{r}_{rbE}, \mathbf{r}_{mrE}, \mathbf{r}_{bE}$	the positions of fixed mass, moving mass, and variable mass in inertial frame	$\mathbf{r}_{rb}, \mathbf{r}_{mr}, \mathbf{r}_b$	the positions of fixed mass, moving mass, and variable mass in body frame
$\mathbf{R}_{e1}$	the matrix rotate around the $\mathbf{e}_1$ axis	r_{mrx}	the component of the $\mathbf{r}_{mr}$ along the $\mathbf{e}_1$ axis
γ	the rotated angle of the movable mass	R_{mr}	the eccentric distance of the moveable mass
$\mathbf{I}_{mr}^0$	the initial inertia matrix when $\gamma = 0$	$\mathbf{I}_{rb}, \mathbf{I}_{mr}, \mathbf{I}_b$	the rotational inertia matrix of fixed mass, moveable/rotateable mass and variable mass
$\mathbf{M}_f, \mathbf{I}_f, \mathbf{D}_f$	the matrix of added mass, added inertial and coupled parameters	$\mathbf{V}_{rb}, \mathbf{V}_{mr}, \mathbf{V}_b$	the velocity of the fixed mass, moving mass and variable mass in inertial frame
$\mathbf{\Omega}_{rb}, \mathbf{\Omega}_{mr}, \mathbf{\Omega}_b$	the angular velocity of the fixed mass, moving mass and variable mass in inertial frame	$\mathcal{I}$	the third order identity matrix
$\mathbf{p}, \boldsymbol{\pi}$	the momentum and angular momentum in inertial frame	$\mathbf{P}, \mathbf{\Pi}$	the momentum and angular momentum in body frame
$\mathbf{f}_{ext}, \boldsymbol{\tau}_{ext}$	the force and moment acting on the vehicle in inertial frame	$\mathbf{F}, \mathbf{T}$	the force and moment acting on the vehicle in body frame
D/X,SF/Y,L/Z	drag, drift force,vertical force	K /T_1,M/T_2,N /T_3	the moment components
K_{L0}, K_L,K_β,K_{D0}, K_D	the coefficients of vertical force ,drift force and drag force	K_{MR}, K_p,K_{M0}, K_M, K_q, K_{MY}, K_r	the coefficients of T_1, T_2, T_3
g	acceleration of gravity	T	the total kinetic energy of the vehicle
T_rb, T_{mr}	the kinetic energy of fixed mass and moving mass	T_b,T_f	the kinetic energy of variable mass and added mass
$\mathbf{u}$	the control input of system	$\mathbf{y}_d$	the target control parameter of the system
μ_i	the estimated value of u_i	z	the difference between the state parameter value and estimated value

References

1. Li, D.H.; Wu, L.X.; Chen, Z.H. Strategic direction and construction path of transparent oceans. *J. Shandong Univ.* **2019**, *2*, 130–136.
2. Liu, Z.H.; Wu, X.F.; Xu, J.P.; Li, H.; Lu, X.L. Fifteen years of ocean observations with China Argo. *Adv. Earth Sci.* **2016**, *31*, 1–16.
3. Rudnick, D.L. Ocean Research Enabled by Underwater Gliders. *Annu. Rev. Mar. Sci.* **2016**, *8*, 519–541. [CrossRef] [PubMed]
4. Cao, J.J.; Li, D.W.; Zeng, Z.; Yao, B.H.; Lian, L. Drifting and Gliding: Design of a multimodal Underwater Vehicle. In Proceedings of the IEEE OCEANS'2018 KOBE, Kobe, Japan, 28–31 May 2018.
5. Zhao, W.T.; Yu, J.C.; Zhang, A.Q. The Cooperative Control Strategy for Underwater Gliders in OceanMesoscale Eddies Observation Task. *Robot* **2018**, *40*, 206–215.
6. Xie, J.; Counillon, F.; Zhu, J.; Bertino, L. Shaoqiong Yang,Yanhui Wang,Yunlong Yi. An eddy resolving tidal-driven model of the South China Sea assimilating along-track SLA data using the EnOI. *Ocean Sci.* **2011**, *7*, 609–627. [CrossRef]
7. Li, Z.; Li, Y.P. Research on thermocline tracking based on dual autonomous underwater vehicles. *Acm Int. Conf. Proc. Ser.* **2018**, *9*, 122–127.
8. Panda, P.J.; Mitra, A.; Warrior, H.V. A review on the hydrodynamic characteristics of autonomous underwater vehicles. *J. Eng. Marit. Environ.* **2021**, *235*, 15–29. [CrossRef]
9. Hwang, J.; Bose, N.; Fan, S.S. AUV adaptive sampling methods: A review. *Appl. Sci.* **2019**, *9*, 3145. [CrossRef]
10. Ullah, B.; Ovinis, M.; Baharom, M.B.; Javaid, M.Y.; Izhar, S.S. Underwater gliders control strategies: A review. In Proceedings of the 2015 10th Asian Control Conference (ASCC), Kota Kinabalu, Malaysia, 31 May–3 June 2015.
11. Graver, J.G. Underwater Glider: Dynamics, Control and Design. Ph.D. Thesis, Princeton University, Princeton, NJ, USA, 2005.

12. Wang, Y.H. Dynamical Behavior and Robust Control Strategies of the Underwater Gliders. Ph.D. Thesis, Tian Jin University, Tian Jin, China, 2007.
13. Wang, S.X.; Liu, F.; Shao, S; Wang, Y.H.; Niu, W.D.; Wu, Z.L. Dynamic modeling of hybrid underwater glider based on the theory of differential geometry and sea trails. *J. Mech. Eng.* **2014**, *50*, 19–27. [CrossRef]
14. Yang, M.; Wang, Y.H.; Yang, S.Q.; Zhang, L.H.; Deng, J.J. Shape optimization of underwater glider based on approximate model technology. *Appl. Ocean Res.* **2021**, *110*, 102580. [CrossRef]
15. Fan, S.S.; Woolsey, C.A. Dynamics of underwater gliders in currents. *Ocean Eng.* **2014**, *84*, 249–258. [CrossRef]
16. Breivik, M.; Fossen, T.I. A unified control concept for autonomous underwater vehicles. In Proceedings of the American Control Conference, Minneapolis, MN, USA, 14–16 June 2006; pp. 4920–4926.
17. Xiang, X.; Yu, C.; Zhang, Q.; Xu, G. Path-following control of an AUV: Fully actuated versus under-actuated configuration. *Mar. Technol. Soc. J.* **2016**, *50*, 34–47. [CrossRef]
18. Niu, W.D. Stability Contorl and Path Planning for Hybrid-Driven Underwater Gliders. Ph.D. Thesis, Tian Jin University, Tian Jin, China, 2016.
19. Noh, M.M.; Arshad, M.R.; Mokhtar, R.M. Depth and pitch control of USM underwater glider: Performance comparison PID vs. LQR. *Indian J. Marine Sci.* **2011**, *40*, 200–206.
20. Isa, K.; Rizal, A.M. Motion simulation for propeller-driven USM underwater glider with controllable wings and rudder. In Proceedings of 2011 2nd International Conference on Instrumentation Control and Automation, ICA, Bandung, Indonesia, 15–17 November 2011; pp. 316–321.
21. Wang, S.; Li, H.; Wang, Y.; Mokhtar, R.M. Dynamic modeling and motion analysis for a dual-buoyancy-driven full ocean depth glider. *Ocean Eng.* **2019**, *187*, 106163. [CrossRef]
22. Yang, M.; Wang, Y.; Wang, S.; Mokhtar, R.M. Motion parameter optimization for gliding strategy analysis of underwater gliders. *Ocean Eng.* **2019**, *191*, 106502. [CrossRef]
23. Yang, H.; Ma, J.; Mokhtar, R.M. Sliding mode tracking control of autonomous underwater glider. In Proceedings of the 2010 International Conference on Computer Application and System Modeling, Taiyuan, China, 22–24 October 2010; Volume 1, pp. 555–558.
24. Liu, Y.; Ma, J.; Huang, Z. Numerical study on hydrodynamic behavior of an underwater glider. *Ocean Eng.* **2011**, *6*, 521–526.
25. Cao, J.; Cao, J.; Zeng, Z. Nonlinear multiple-input-multiple-output adaptive backstepping control of underwater glider systems. *Int. J. Adv. Robot. Syst.* **2016**, *13*, 1–14. [CrossRef]
26. Cao, J.J.; Lu, D.; Li, D.W.; Zeng, Z.; Yao, B.H.; Lian, L. Smartfloat: A Multimodal Underwater Vehicle Combining Float and Glider Capabilities. *IEEE Access* **2019**, *7*, 77825–77838. [CrossRef]
27. Zhang, R.; Yang, S.; Wang, Y.; Yi, Y. Regional ocean current field construction based on an empirical bayesian kriging algorithm using dual underwater gliders. *J. Coast. Res.* **2020**, *99*, 41–47. [CrossRef]
28. Xiao, H.; Zhang, Z.; Chen, L.; He, Q. An Improved Spatio-Temporal Kriging Interpolation Algorithm and Its Application in Slope. *IEEE Access* **2020**, *8*, 90718–90729. [CrossRef]